

MPF-Bench : A Large Scale Dataset for SciML of Multi-Phase Flows: Droplet and Bubble Dynamics

Mehdi Shadkhah¹

MEHDISH@IASTATE.EDU

Ronak Tali^{1†}

RTALI@IASTATE.EDU

Ali Rabeh^{1†}

ARABEH@IASTATE.EDU

Cheng-Hau Yang^{1†}

CHENGHAU@IASTATE.EDU

Ethan Herron^{1†}

EDHERRON@IASTATE.EDU

Abhisek Upadhyaya²

AU2216@NYU.EDU

Adarsh Krishnamurthy¹

ADARSH@IASTATE.EDU

Chinmay Hegde²

CHINMAY.H@NYU.EDU

Aditya Balu¹

BADITYA@IASTATE.EDU

Baskar Ganapathysubramanian^{1*}

BASKARG@IASTATE.EDU

¹Department of Mechanical Engineering, Iowa State University, Ames, IA 50011, USA

²Department of Computer Science and Engineering, New York University, New York, NY 10012, USA

Reviewed on OpenReview: <https://openreview.net/forum?id=9gQnIFI4es¬eId=JNLXJbCwZq>

Editor: Yi Liu

Abstract

Multiphase fluid dynamics, such as falling droplets and rising bubbles, is critical for many industrial applications. However, simulating these phenomena efficiently is challenging due to the complexity of instabilities, wave patterns, and bubble breakup. This paper investigates the potential of scientific machine learning (SciML) to model these dynamics using neural operators and foundation models. We apply sequence-to-sequence learning techniques to a comprehensive dataset of 11,000 simulations, which includes over 1 million time snapshots, generated using a well-validated, CUDA-accelerated Lattice Boltzmann Method (LBM) framework. The results demonstrate the ability of machine learning models to capture transient dynamics and intricate fluid interactions, paving the way for more accurate and computationally efficient SciML-based solvers for multiphase applications.

Keywords: Scientific Machine Learning, Multiphase Flow Simulation, Neural Operators, vision transformers (ViT), Bubble and Droplet Dynamics, Benchmark Dataset

1 Introduction

Flow behavior in multiphase systems is crucial for many industrial and chemical applications. In drug delivery applications, two-phase flow can be used to create uniformly microspheres or microcapsules. These microcapsules can provide controlled and sustained release of drugs, improving therapeutic results (Hernot and Klibanov, 2008; Sattari et al., 2020). Two-phase flows are also essential for rapid diagnostics and biochemical applications in lab-on-a-chip technologies (Haeberle and Zengerle, 2007; Mark et al., 2010). Discrete bubbles in

*, † Equal contribution. * Corresponding author.

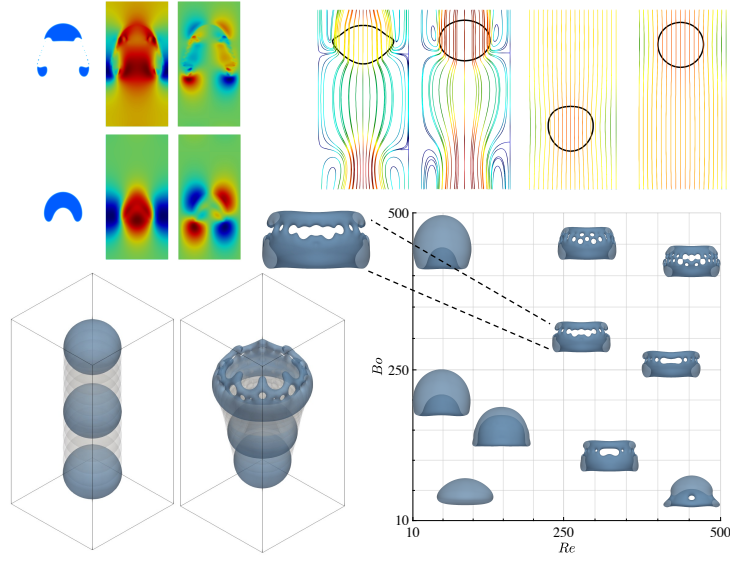


Figure 1: *MPF-Bench* includes 11,000 two-phase flow simulations. The top left panel displays velocity results in both x and y directions and bubble shapes for two randomly selected 2D bubble rising simulations. The top right panel presents 2D droplet falling simulations, depicting streamlines colored by velocity magnitude and droplet shapes. The bottom left panel illustrates 3D simulation outputs, highlighting time series outputs from our dataset. The bottom right panel shows 3D bubble shapes for different Reynolds and Bond number combinations.

microchannels, generated via T-junctions (Thorsen et al., 2001), co-flowing systems (Cramer et al., 2004), or flow-focusing techniques (Anna et al., 2003), have a high surface-to-volume ratio, which improves the reaction efficiency and sensitivity. The shearing forces of the continuous phase precisely control the size and formation of the bubble, which is crucial for device performance. By thoroughly understanding the gas-liquid or liquid-liquid interactions, engineers can optimize mixing conditions (Schwesinger et al., 1996; Stroock et al., 2002; Tice et al., 2003) to enhance reaction rates, improve product consistency, and reduce energy consumption.

Bubbles (*lighter fluid volumes moving in a denser fluid medium*) and droplets (*heavier fluid volumes moving in a lighter fluid medium*) play an integral role in applications such as drug delivery and lab-on-a-chip technologies. The dynamics of droplets and bubbles exhibit significant complexity, primarily due to phenomena such as breakup, deformation, and surface tension. Firstly, the breakup of droplets and bubbles is a highly nonlinear and complex process governed by factors such as the viscosity ratio, density ratio, and surface tension. For example, for high-inertia flows, the fast and irregular breakup results in smaller and distributed droplets; at low Reynolds numbers, laminar flow leads to a more even breakup and larger droplets (Eggers and Villermaux, 2008). Secondly, droplets can be deformed by shear and pressure forces. Various studies have shown that the Capillary number (Vananroye et al., 2008; Liu et al., 2022), Atwood number (Fakhari and Rahimian, 2010; Singh, 2020), and Reynolds number (Vontas et al., 2020; Xu et al., 2020; Seksinsky and Marshall, 2021) all have a significant impact on droplet deformation.

To better understand multiphase phenomena (both droplets and bubbles), researchers often perform a canonical simulation/experiment called the bubble rising case (Bhaga and Weber, 1981b; Hua and Lou, 2007; Hysing et al., 2009; Amaya-Bower and Lee, 2010; Aland and Voigt, 2012; Yuan et al., 2017; Khanwale et al., 2023; Rabeh et al., 2024b), where a bubble is placed in a higher density fluid so that the bubble moves up due to buoyancy. Conversely, using a droplet of higher density causes the droplet to fall down due to gravity (Yang et al., 2021; Jalaal and Mehravaran, 2012). This canonical study is essential since it provides insights into bubble dynamics and shape evolution, which are critical factors for optimizing industrial processes and improving numerical models in fluid dynamics research. Nonetheless, capturing the bubble rising or droplet falling phenomenon is a multiscale problem with forces acting at different scales, ranging from microscale molecular interactions to macroscale fluid dynamics. Therefore, high-fidelity simulations are essential to accurately resolve these interactions, particularly at the thin interfaces where precise capturing of surface tension and interfacial dynamics is critical.

Scientific Machine Learning (SciML) represents a powerful approach to address multiphase flow problems. SciML leverages the inherent physics to develop models that can learn from complex data and produce reliable predictions (Karniadakis et al., 2021; Hassan et al., 2023; M Silva et al., 2024; Rabeh et al., 2024a). A key ingredient for training and accessing SciML solvers is a comprehensive dataset that can thoroughly test the ability of SciML models (Tali et al., 2024). In this regard, **MPF-Bench** is a benchmark dataset that includes wave patterns, bubble and droplet dynamics, as well as breakup phenomena.

There are several approaches to using machine learning to solve scientific problems, including Physics-Informed Neural Networks (PINNs) (Raissi et al., 2019) and neural operators (Li et al., 2021; Raonić et al., 2023; Lu et al., 2021). However, PINNs suffer from hard convergence and high generalization error (Rathore et al., 2024). In this paper, we focus on using neural operators and foundation models. **MPF-Bench** has three major features:

- **Scientific machine learning evaluations:** We test our dataset on several neural operators and foundation models using the sequence-to-sequence time series concatenation technique. Our dataset serves as a good test for these models to evaluate their ability to learn multiscale physics data.
- **Extensive amount of data:** Our dataset includes 11,000 simulations in 2D and 3D with over 1 million time-series snapshots. This extensive volume of data allows for robust training of SciML models, which will help in advancing the development of accurate and reliable SciML models for multiphase flow dynamics.
- **Multiphase simulations:** We conduct simulations of rising bubbles and falling droplets, solving the Navier-Stokes equations coupled with the Allen-Cahn equation. This approach captures considerable physical phenomena, including breakup and deformation.

Our contributions: We summarize our main contributions below:

- We perform a comparative benchmark of six neural operators and foundation models trained on our data, i.e., predicting interface, velocity, and pressure solution fields using previous time snapshots as inputs to the models. Although recent works have applied operator learning to bubble and droplet dynamics (Lin et al., 2021b,a; Sanchez-Gonzalez

et al., 2020), there have been no prior comparative benchmarks that include foundation models on a large-scale multiphase dataset to the best of our knowledge.

- Our dataset features 11,000 simulations and over 1 million time-series snapshots, with variations in density ratio, viscosity ratio, Reynolds number, and Bond number. This extensive dataset encompasses many phenomena, ranging from subtle surface deformations in bubble oscillations to full bubble breakups driven by surface tension and density ratio variations.

The richness and breadth of this dataset offer deep insights into the intricate dynamics of multiphase flows, making it a valuable resource for advancing research in this field. We provide our [dataset](#) as a benchmark for others interested in developing and evaluating SciML models. Additional details can also be found in our [website](#).

2 Related Work

The Stanford Multiphase Flow Database (SMFD) used in (Chaari et al., 2018), the flow experiment dataset (Al-Dogail and Gajbhiye, 2021), and the BubbleML dataset (Hassan et al., 2023) are resources for understanding multiphase flow dynamics. The SMFD features 5659 measurements across a range of gas and liquid properties, pipe characteristics, and operational conditions. This dataset, derived from laboratory and field sources, supports various pipe inclinations and flow patterns. SMFD covers different flow regimes, including stratified, slug, and annular flows. However, it does not appear publicly available, so we cannot identify the number of individual snapshots in this dataset.

The flow experiment dataset (Al-Dogail and Gajbhiye, 2021) focuses on the effects of density, viscosity, and surface tension on two-phase flow regimes and pressure drops in

Table 1: Comparison of public Multiphase Flow Datasets. A sample refers to one full simulation case, such as a single bubble-rising experiment. Each sample includes multiple snapshots, where a snapshot is the solution field at one time step.

Name	Samples	Snapshots	Scope	Sources	Ranges of material properties
Flow Experiment Dataset	2904	2904	Horizontal pipes, effects of density, viscosity, surface tension	Controlled lab environment	ρ : [1, 1.5] gm/cc, μ : [1, 3.1] cP, Surface tension = [32, 70] mN/m
BubbleML	79	7641	pool boiling, flow boiling, and sub-cooled boiling	2D and 3D numerical simulations based on Flash-X	Re = 0.0042, ρ^* = 0.0083, μ^* = 1, Pr = 8.4, We = 1, Fr = [1, 100]
MPF-Bench	11,000	> 1 million	Droplet and bubble dynamics	2D and 3D simulations using LBM	ρ^* : [10, 1000], μ^* : [1, 100], Bo : [10, 500], Re : [10, 1000]

horizontal pipes. The 2904 air–liquid system measurements reveal how fluid properties affect flow regimes and pressure drops. This dataset’s flow regime classifications and pressure contour maps improve understanding of fluid behavior in horizontal two-phase flows. Additionally, the BubbleML dataset (Hassan et al., 2023) is a data collection focused on multiphysics phase change phenomena generated through physics-driven simulations, providing ground truth information for various boiling scenarios, including nucleate pool boiling, flow boiling, and sub-cooled boiling. We summarize these and other databases alongside our dataset in Table 1.

Recent operator-learning approaches have also focused on learning multiphase dynamics. For example, Lin et al. (2021b) developed multiscale DeepONet architectures that accurately infer bubble shape evolution across varying density and viscosity ratios, demonstrating strong generalization even under out-of-distribution conditions. Similarly, Sanchez-Gonzalez et al. (2020) employed graph-network–based simulators to learn fluid interactions in complex physics domains, capturing local phase interfaces and long-range coupling effects. These pioneering efforts illustrate the feasibility of operator learning for multiphase settings and motivate our benchmark of multiple neural operators and foundation models on a large-scale dataset.

3 Multi-phase flow (MPF) Bench

We present the **MPF-Bench** dataset, encompassing 5500 bubble rise and 5500 droplet flow simulations, with each simulation containing 100 time-snapshots, making it, to our knowledge, two orders of magnitude larger – in terms of number of time-snapshots – than any existing multiphase flow dataset. This dataset features 2D and 3D transient simulations, capturing a spectrum of flow behaviors influenced by surface tension and density/viscosity ratios. **MPF-Bench** includes scenarios from bubble oscillations with minor surface deformations to complete bubble breakup, offering a comprehensive resource for studying bubble rise and droplet fall dynamics.

3.1 Problem Definition: Initial and Boundary Conditions, and outputs

We consider 2D and 3D simulations of bubble rise and droplet fall using the lattice Boltzmann method. The computational domain spans $[256, 512]$ lattice units in 2D and $[128, 256, 128]$ in 3D, corresponding to the (x, y) and (x, y, z) directions, respectively. In 2D, the bubble is initially centered at $(x, y) = (64, 64)$, and the droplet at $(128, 384)$. In 3D, the bubble is centered at $(x, y, z) = (64, 64, 64)$, and the droplet at $(64, 192, 64)$. The initial diameter D_0 is set to 128 lattice units in 2D and 64 lattice units in 3D for both problems. The boundary conditions are set to free-slip on the side walls and periodic at the top and bottom as illustrated in Figure 2. This problem is driven mainly by the density and viscosity ratio of the two phases, along with the Reynolds and Bond numbers. The Reynolds number measures the ratio of inertial forces to viscous forces, while the Bond number measures the ratio of gravitational forces to surface tension forces. Below is the definition of these four dimensionless numbers:

$$\rho^* = \frac{\rho_h}{\rho_l}, \quad \mu^* = \frac{\mu_h}{\mu_l}, \quad \text{Re}_h = \frac{\sqrt{g_y \rho_h (\rho_h - \rho_l) D^3}}{\mu_h}, \quad \text{Bo} = \frac{g_y (\rho_h - \rho_l) D^2}{\sigma} \quad (1)$$

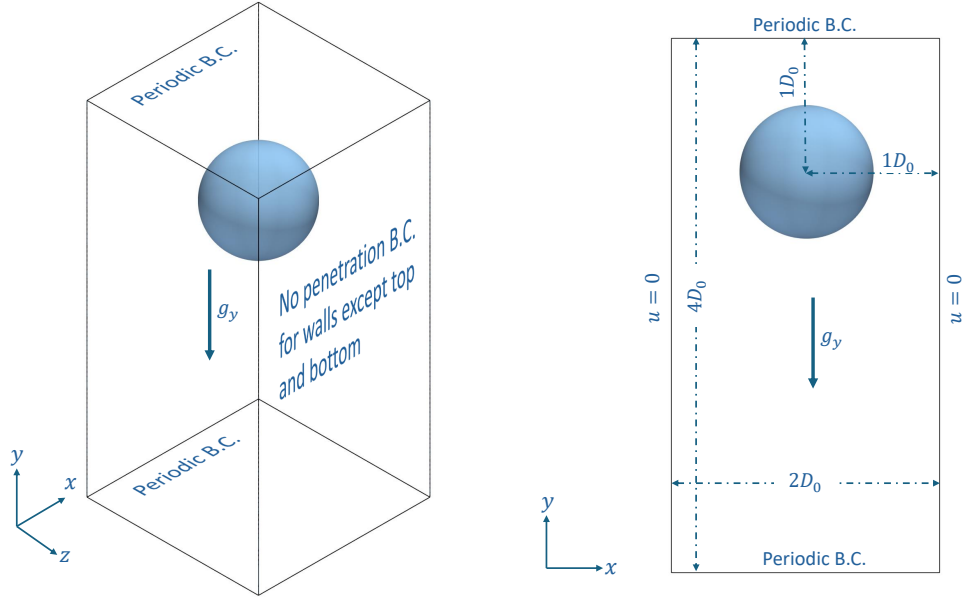


Figure 2: Boundary conditions for the simulation of a falling droplet. The left panel illustrates the 3D case, while the right panel illustrates the 2D case.

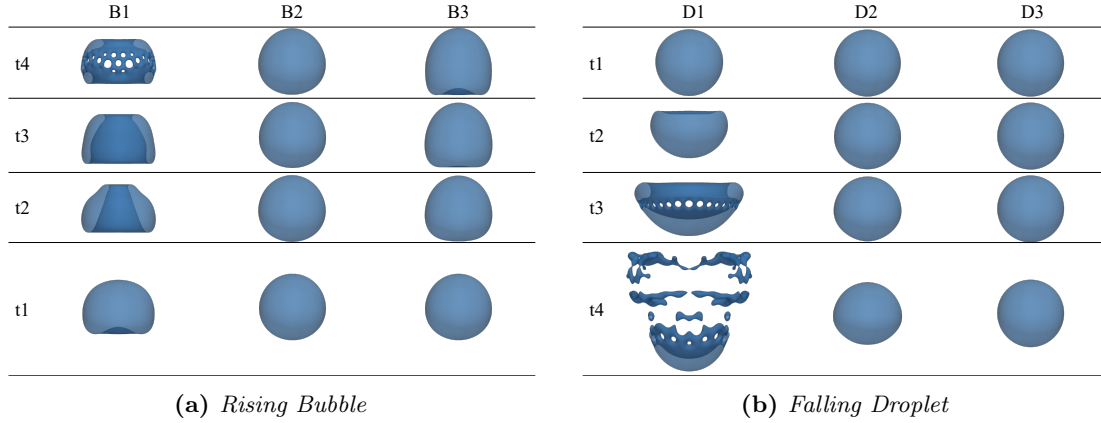


Figure 3: (a) Snapshot of a 3D rising bubble and (b) snapshot of a 3D falling droplet. The properties of the fluids for each case are detailed in [Table 2](#).

where h and l indices refer to the heavy and light fluids, respectively. We uniformly sampled the dimensionless numbers to cover the full defined range. The outputs of the simulations are the interface indicator (c), velocity components (u, v, w), pressure (p), and density (ρ) which provide insights into the dynamics of multiphase flow and the interactions between the phases.

We selected a few representative cases from our dataset to illustrate the key physics of droplet and bubble dynamics (see [Table 2](#)). As shown in [Figure 3](#) and [Figure 5](#), these cases highlight how variations in Bond number, Reynolds number, and density ratio affect droplet deformation and breakup patterns. Each case reveals distinct fluid behaviors, enhancing our

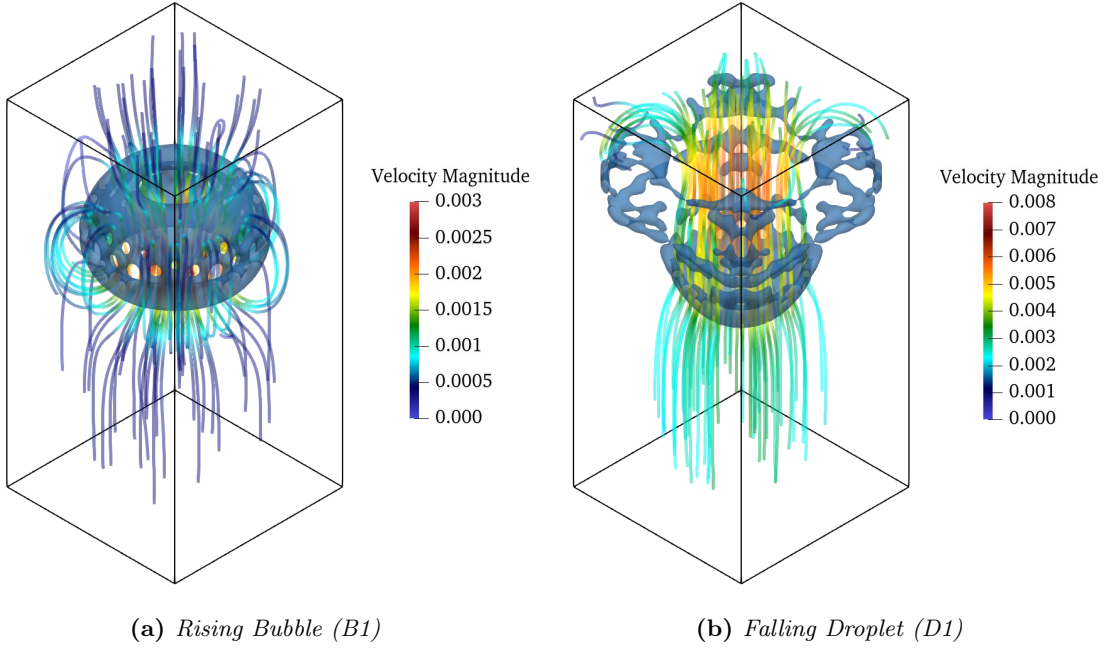


Figure 4: Streamlines of a 3D rising bubble (a) and a 3D falling droplet (b), with color indicating the magnitude of velocity. The properties of the fluids for each case are detailed in [Table 2](#).

understanding of the complex, nonlinear dynamics. The streamlines around the bubble and

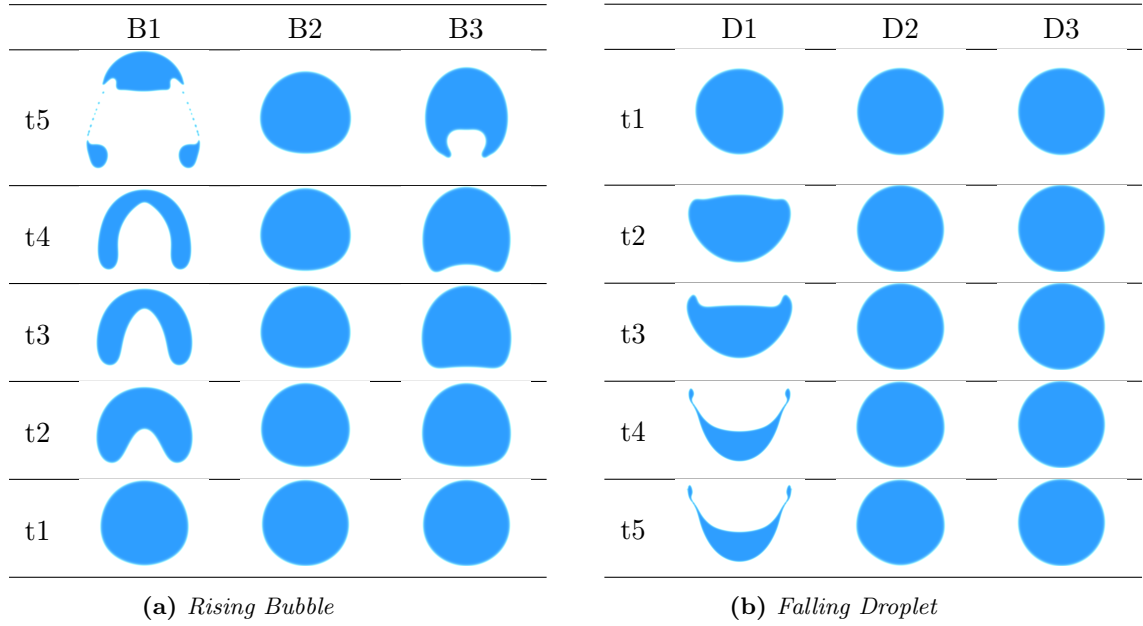


Figure 5: (a) Snapshot of a 2D rising bubble and (b) snapshot of a 2D falling droplet. The properties of the fluids for each case are detailed in [Table 2](#).

Table 2: Material properties and nondimensional numbers of three bubble rise simulations ($B1$, $B2$, $B3$) and three droplet fall simulations ($D1$, $D2$, $D3$). The table shows the density ratio, viscosity ratio, Reynolds number, and Bond number of all six simulations.

case	B1	B2	B3	D1	D2	D3
Density Ratio (ρ^*)	10^3	10^3	10^3	10	10^3	10^3
Viscosity Ratio (μ^*)	10^2	10^2	10^2	1	10^2	10^2
Re	5×10^2	10	10	10^3	10^3	10
Bo	5×10^2	10	5×10^2	5×10^2	5×10^2	10

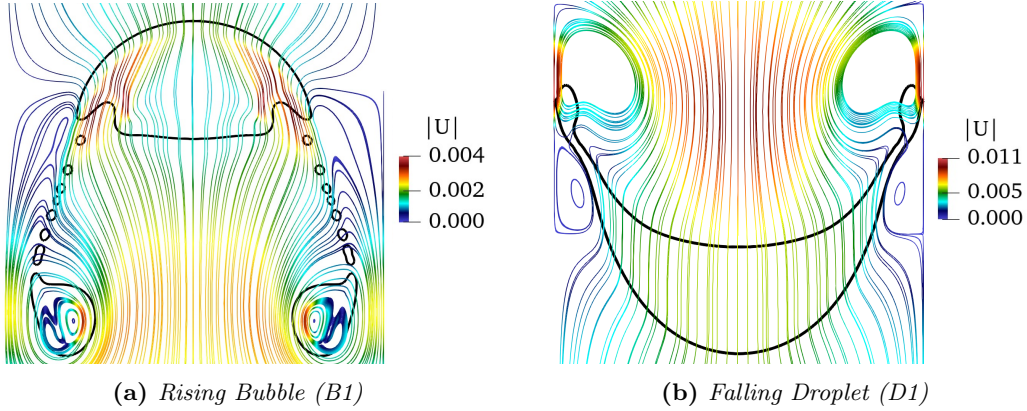


Figure 6: Streamlines of a 2D rising bubble (a) and a 2D falling droplet (b), with colors indicating the magnitude of velocity.

droplet, depicted in Figure 4 and Figure 6, further illustrate how these physical parameters influence droplet breakup and stability across 3D and 2D flows.

3.2 Simulation Framework and Compute Effort

Our simulation framework employs [CLIP](#), a CUDA-accelerated Lattice Boltzmann framework that incorporates a phase-field two-phase model to capture complex interfacial dynamics (Shadkhah et al., 2025). The code has been rigorously tested across various problems, with validation results provided in [Section A.3](#). For 2D simulations, we used a uniform lattice grid of 256×512 , while for 3D simulations, the domain was set to $128 \times 256 \times 128$. We achieved high parallelization by distributing the computation across 12 NVIDIA A100-SXM4 80GB GPUs. The total computational cost for 2D and 3D cases was approximately 4,000 GPU hours. We use the ParaView tool (Ayachit, 2015) to visualize and understand our dataset.

3.3 MetaData

Input Fields: We use the following dimensionless quantities as inputs, as defined in [Section 3.1](#). These are the Density Ratio (ρ^*), Viscosity Ratio (μ^*), Bond Number (Bo), and Reynolds Number (Re). Since these are scalar values, we feed them to the neural network by creating a constant field with a dimension consistent with the number of samples, in this case, 10,000 in 2D and 1,000 in 3D.

Output Fields: In analyzing multiphase flow problems, we are interested in solving the governing PDEs to obtain solutions at every point in the domain’s interior for certain cardinal fields. For a 2D solution domain, these are: c - interface indicator, u - velocity in x direction, v - velocity in y direction, p - pressure. As this is a time-dependent problem, each simulation is run for 400,000 time steps using a uniform lattice time step of $\Delta t = 1$ (in lattice units), with cardinal fields recorded as time series. For 2D simulations, we store one output every 4,000 time steps, yielding 100 uniformly distributed snapshots per simulation. For 3D simulations, outputs are stored every 8,000 time steps, resulting in 50 snapshots per case. These time series capture the temporal evolution of key fields across the domain. Readers interested in converting simulation time to physical time can refer to [Equation 18](#) in the [Section A](#), which provides the necessary dimensionless scaling.

Resolution: We maintained the original resolution of our datasets, matching the Lattice Boltzmann simulation domain. This ensures the complete physics is presented to the neural operator and allows direct comparison with Lattice Boltzmann method simulations. Our datasets are published at 256×512 resolution for 2D and $128 \times 256 \times 128$ for 3D simulations.

Dataset Format: For both the bubble and droplet datasets, we have released a single file for each sample. This decision was taken to allow maximum flexibility in choosing which time-steps to use for training, since these problems are inherently sequence-to-sequence. In 2D, the resulting .npz files take the form:

$$[\mathbf{T}][\mathbf{C}][\mathbf{H}][\mathbf{W}]$$

where \mathbf{T} is the number of time steps, \mathbf{C} is the number of channels (e.g., physical variables such as velocity components or phase fields), \mathbf{H} is the resolution in the vertical direction (height or y -axis), and \mathbf{W} is the resolution in the horizontal direction (width or x -axis). In 3D datasets, an additional dimension \mathbf{D} is included to represent the depth or resolution in the z -direction:

$$[\mathbf{T}][\mathbf{C}][\mathbf{D}][\mathbf{H}][\mathbf{W}]$$

Table 3: Formulaic description of the input and output tensors. 5000 - sample size for the dataset. 101 - number of time steps in the simulation. x, y - The x, y dimension of a field. E.g., $Y[0, 100, 1, :, :]$ indicates the pointwise v velocity over the entire grid of size 256×512 for the first sample at time step 100.

Dataset	Dim.	Input Tensor	Output Tensor
Droplet	2	$X[5000][\rho^*, \mu^*, Bo, Re]$	$Y[5000][101][c, u, v, p, \rho][y][x]$
Bubble	2	$X[5000][\rho^*, \mu^*, Bo, Re]$	$Y[5000][101][c, u, v, p, \rho][y][x]$
Droplet	3	$X[500][\rho^*, \mu^*, Bo, Re]$	$Y[500][51][c, u, v, w, p, \rho][z][y][x]$
Bubble	3	$X[500][\rho^*, \mu^*, Bo, Re]$	$Y[500][51][c, u, v, w, p, \rho][z][y][x]$

Table 4: Dataset parameters with difficulty levels for selecting appropriate cases based on Reynolds number, density ratio, viscosity ratio, and Bond number.

Density Ratio	Viscosity Ratio	Bo Number	Re Number	Difficulty
High	High	High	High	Challenging
High	High	Low	Low	Easy
High	High	Low	Low	Moderate
High	High	Low	High	Moderate
High	High	High	High	Challenging
Low	Low	High	High	Challenging
Low	Low	Low	Low	Easy
Low	Low	High	High	Easy
Low	Low	Low	High	Moderate

In this study, we have released a total of 11,000 samples spread across two families of datasets. Table 3 presents a detailed structural description of how the input and output NumPy tensors are organized for both dataset families.

Level of Difficulty: We provide Table 4 to help users select datasets based on varying difficulty levels. The dataset includes key parameters like Reynolds number (Re), Density Ratio, Viscosity Ratio, and Bond Number (Bo), with a difficulty classification to guide users. The classification into “High” and “Low” is based on a rough quantile-based estimate using the parameter ranges provided in Table 2: the upper 40% of each parameter’s range is labeled as “High,” and the lower 40% as “Low.” The remaining middle 20% is considered transitional, where classification may vary. This categorization reflects the complexity of interface deformations, making it easier to choose suitable cases for model training and evaluation.

3.4 Evaluation Metrics and Test Dataset Analysis

We assess the performance of the trained neural operators and foundation models using two primary metrics: Mean Squared Error (MSE) and relative L_2 error. To capture the transient behavior of the system, we employ both sequence-to-sequence and sequence-to-field mappings, where solution fields at various time steps are concatenated and passed sequentially into the

models. For training and evaluation, we randomly sampled 1,000 trajectories from the full 2D bubble dataset, focusing on cases labeled with “Easy” and “Moderate” difficulty levels. The exact dataset splits used for scenarios $S1$ – $S6$ are publicly available at [Hugging Face](#).

The dataset consists of 100 temporal snapshots of bubble dynamics. However, to capture stronger temporal variations, we choose every fourth time step, thereby reducing our time series to 25 snapshots for each case. For instance, $t3$ in our evaluation aligns with the 12th time step in the original 100-snapshot dataset. This approach ensures the input sequences contain larger changes in the bubble’s shape and velocity fields, thereby increasing the learning challenge for the machine learning models. By skipping every fourth timesteps, we ensure the models learn from substantial temporal variations rather than minor changes, ultimately making the learning problem more challenging for capturing multi-phase flow dynamics.

The models are evaluated on six distinct input-output mappings ($S1$ through $S6$) as outlined below:

- **Sequence-to-field:** We set up three different input scenarios for subsets $S1$, $S2$, and $S3$. In these cases, the goal is to predict a single future time step given past information. The input consists of solution fields at:
 - $t1$, which represents the first time snapshot in the reduced dataset.
 - A short sequence from $t1$ to $t3$.
 - A longer sequence from $t1$ to $t5$.

For each case, the model predicts the immediate next timestep in the reduced dataset, i.e., $t2$ for $S1$, $t4$ for $S2$, and $t6$ for $S3$.

- **Sequence-to-sequence:** In this case, the output is not a single time snapshot but a sequence of solutions. The goal is to predict multiple future time steps, capturing the evolving dynamics of the bubble rise. We input solution sequences of:
 - $t1$ to $t3$, corresponding to the first three selected snapshots.
 - $t1$ to $t5$, an extended sequence covering more temporal context.
 - $t1$ to $t8$, further increasing the sequence length to capture longer-term dependencies.

For each case, the model predicts a sequence of three future timesteps. Specifically, the outputs for $S4$, $S5$, and $S6$ are the next three consecutive time snapshots after the given input sequence.

This evaluation framework allows us to test the models’ ability to generalize across different temporal dependencies, ranging from short-term extrapolations in sequence-to-field tasks to longer-term sequence predictions in sequence-to-sequence tasks.

The dataset used for these tasks ($S1$ – $S6$) is available on [HuggingFace](#) under the directory `2Dbubble/mpf_paper_dataset`. This folder contains the following files corresponding to each scenario from $S1$ through $S6$: `d#X_train_pad_flat.npz`, `d#Y_train_pad_flat.npz`, `d#X_test_pad_flat.npz`, and `d#Y_test_pad_flat.npz`.

3.5 Dataset Format

We store all training and testing data for the six input-output mappings ($S1$ to $S6$) in `.npz` files. Each `.npz` file contains a single NumPy array named `Y` of shape (N, C, H, W) , where:

- N is the number of samples (800 for training, 200 for testing).
- C is the total number of channels, determined by the number of time snapshots \times physical fields. For instance, in a sequence-to-sequence task with 8 input snapshots (each containing 4 fields), $C = 8 \times 4 = 32$.
- H and W are the spatial dimensions, fixed at 256×256 for these simulations.

For example, `d6X_train_pad_flat.npz` has shape $(800, 32, 256, 256)$ because $S6$ requires an 8-snapshot input (each snapshot with 4 channels). Similarly, the corresponding output `d6Y_train_pad_flat.npz` has shape $(800, 12, 256, 256)$, where 12 channels correspond to 3 future snapshots \times 4 fields each. The same mapping applies to `d1X_train_pad_flat.npz`, `d1Y_train_pad_flat.npz`, etc., with varying numbers of channels depending on how many time snapshots each mapping ($S1$ to $S6$) requires.

4 Experiments

Neural operators represent a class of deep learning methods designed to learn function spaces of solutions to partial differential equations (PDEs). Unlike traditional deep learning methods, which focus on finding a parametric solution for a fixed problem, Neural Operators are capable of generalizing to solutions of PDEs. While these frameworks have demonstrated notable success in modeling single-phase fluid flow, there is limited research on their ability to capture multiphase flows. Multi-phase flows present additional challenges due to phenomena like bubble or droplet breakup, coalescence, and shape oscillations. In this context, we aim to evaluate the performance of several Neural Operators and foundation models in learning these intricate fluid dynamics.

We provide baseline results by training a range of well-established neural PDE solvers, commonly referred to as scientific machine learning (SciML) models. Specifically, we examined the following neural operators and transformer-based foundation models on the 2D bubble benchmark: (a) Fourier Neural Operator (FNO) (Li et al., 2021), (b) Convolutional Neural Operators (CNO) (Raonić et al., 2023), (c) DeepONet (Lu et al., 2021), (d) UNet (Ronneberger et al., 2015), (e) scOT (a randomly initialized vision-based transformer) (Li et al., 2023), (f) Poseidon (a pre-trained, vision-based foundation model) (Herde et al., 2024). For training, we closely followed the published code examples, and the code used for training these models is available in the following GitHub repository: [GitHub](#). All models were trained for 200 epochs on a single A100 80GB GPU using the Adam optimizer, and the hyperparameter settings for each model are detailed in [Section B.1](#). The validation loss for all models converged by 200 epochs, and the training and validation loss curves for two representative models are shown in [Section B.2](#).

[Table 5](#) and [Table 6](#) compare the Mean Squared Error (MSE) and relative L_2 error for sequence-to-field and sequence-to-sequence predictions across various models on the six bubble rise datasets ($S1$ - $S6$). These results highlight the performance differences between models in

Table 5: Comparison of mean squared error (MSE) and relative L_2 error for Sequence-to-Field predictions using UNet, DeepONet, FNO, CNO, scOT, and Poseidon on Bubble Datasets (S1–S3).

Model	Channel	S1		S2		S3	
		MSE	L_2	MSE	L_2	MSE	L_2
UNet	c	2.60×10^{-2}	2.59×10^{-2}	8.40×10^{-3}	8.07×10^{-3}	9.56×10^{-3}	9.04×10^{-3}
	u	8.80×10^{-5}	3.13×10^0	8.00×10^{-6}	2.04×10^0	1.00×10^{-5}	2.09×10^0
	v	1.00×10^{-6}	1.56×10^0	1.00×10^{-6}	7.84×10^{-1}	1.00×10^{-6}	8.76×10^{-1}
	p	1.00×10^{-6}	2.74×10^2	1.00×10^{-6}	3.23×10^2	1.00×10^{-6}	5.17×10^2
DeepONet	c	2.66×10^{-2}	2.65×10^{-2}	1.01×10^{-1}	1.01×10^{-1}	1.18×10^{-1}	1.18×10^{-1}
	u	9.10×10^{-5}	6.71×10^0	1.27×10^{-3}	1.24×10^0	1.71×10^{-3}	9.18×10^{-1}
	v	1.00×10^{-6}	8.68×10^{-1}	1.00×10^{-6}	5.35×10^{-1}	1.00×10^{-6}	8.89×10^{-1}
	p	1.00×10^{-6}	1.89×10^2	1.00×10^{-6}	2.43×10^2	1.00×10^{-6}	1.66×10^2
FNO	c	2.72×10^{-2}	2.68×10^{-2}	9.73×10^{-3}	8.97×10^{-3}	2.10×10^{-2}	1.98×10^{-2}
	u	9.30×10^{-5}	8.56×10^0	1.00×10^{-5}	2.77×10^0	4.80×10^{-5}	5.29×10^0
	v	1.00×10^{-6}	3.43×10^0	1.00×10^{-6}	1.09×10^0	2.00×10^{-6}	2.02×10^0
	p	1.00×10^{-6}	7.18×10^2	1.00×10^{-6}	7.44×10^2	2.00×10^{-6}	1.04×10^3
CNO	c	2.62×10^{-2}	2.60×10^{-1}	5.89×10^{-3}	5.65×10^{-3}	9.41×10^{-3}	9.00×10^{-3}
	u	8.80×10^{-5}	5.04×10^0	4.00×10^{-6}	1.60×10^0	1.00×10^{-5}	1.79×10^0
	v	1.00×10^{-6}	1.73×10^0	1.00×10^{-6}	5.07×10^{-1}	1.00×10^{-6}	9.19×10^{-1}
	p	1.00×10^{-6}	4.46×10^2	1.00×10^{-6}	2.24×10^2	1.00×10^{-6}	3.96×10^2
scOT	c	2.76×10^{-2}	2.68×10^{-2}	1.77×10^{-2}	1.68×10^{-2}	2.23×10^{-2}	2.17×10^{-2}
	u	1.29×10^1	1.29×10^1	3.50×10^{-5}	3.91×10^0	5.80×10^{-5}	2.82×10^0
	v	5.24×10^0	5.24×10^0	1.00×10^{-6}	2.31×10^0	1.00×10^{-6}	1.75×10^0
	p	9.65×10^2	9.65×10^2	2.00×10^{-6}	8.12×10^2	2.00×10^{-6}	7.80×10^2
Poseidon	c	2.87×10^{-2}	2.79×10^{-1}	3.34×10^{-2}	3.01×10^{-2}	2.49×10^{-2}	2.23×10^{-2}
	u	1.00×10^{-4}	1.16×10^1	1.14×10^{-4}	1.31×10^1	6.10×10^{-5}	8.28×10^0
	v	2.00×10^{-6}	5.86×10^0	1.10×10^{-5}	4.05×10^0	5.00×10^{-6}	2.83×10^0
	p	2.00×10^{-6}	1.04×10^3	6.00×10^{-6}	2.35×10^3	4.00×10^{-6}	1.94×10^3

predicting the solution fields for different data subsets (S1–S6). All model predictions improve as more time snapshots are incorporated, reinforcing the importance of temporal context in learning transient phenomena. Additionally, CNO generally outperforms the other models in predicting the concentration field, making it particularly effective for modeling sharp gradients in the interface region. Another interesting observation is that scOT marginally outperforms the pre-trained version of Poseidon. This suggests that Poseidon, having been pretrained exclusively on single-phase flow, struggles to generalize to multi-phase phenomena, highlighting the limitations of transfer learning when faced with physics characterized by sharp gradients near the interface. This performance gap underscores the importance of dataset diversity in foundation models designed for physics-informed learning.

Furthermore, [Figure 7](#) and [Figure 8](#) illustrate field predictions of the concentration field C using UNet, CNO, DeepONet, and Poseidon for sequence-to-field and sequence-to-sequence scenarios, respectively. These figures show that DeepONet performs poorly in both the sequence-to-field and sequence-to-sequence scenarios. Additionally, UNet’s accuracy declines as the prediction horizon extends to longer time sequences, as shown in [Figure 8](#). This suggests that convolution-based architectures may not effectively capture long-range dependencies crucial for tracking evolving multi-phase interfaces over time. In contrast, CNO consistently delivers the best performance in both sequence-to-field and sequence-to-sequence predictions. Its strong performance may be attributed to its ability to blend convolutional representations with continuous function approximations, allowing it to better capture

Table 6: Comparison of mean squared error (MSE) and relative L_2 error for Sequence-to-Sequence predictions using UNet, DeepONet, FNO, CNO, scOT, and Poseidon on Bubble Datasets (S_4 - S_6).

Model	Channel	S4		S5		S6	
		MSE	L_2	MSE	L_2	MSE	L_2
UNet	c	3.27×10^{-2}	2.87×10^{-2}	3.93×10^{-2}	3.31×10^{-2}	7.34×10^{-2}	6.58×10^{-2}
	u	1.35×10^{-4}	3.54×10^0	2.02×10^{-4}	3.10×10^0	6.65×10^{-4}	3.90×10^0
	v	1.00×10^{-6}	1.38×10^0	1.00×10^{-6}	1.45×10^0	1.00×10^{-6}	9.54×10^{-1}
	p	1.00×10^{-6}	6.76×10^2	1.00×10^{-6}	6.30×10^2	1.00×10^{-6}	7.79×10^2
DeepONet	c	1.64×10^{-1}	1.60×10^{-1}	2.03×10^{-1}	1.99×10^{-1}	1.94×10^{-1}	1.92×10^{-1}
	u	3.33×10^{-3}	3.15×10^0	5.04×10^{-3}	1.64×10^0	4.57×10^{-3}	1.32×10^0
	v	1.00×10^{-6}	1.04×10^0	1.00×10^{-6}	7.59×10^{-1}	1.00×10^{-6}	3.83×10^{-1}
	p	1.00×10^{-6}	7.30×10^2	1.00×10^{-6}	3.53×10^2	1.00×10^{-6}	3.17×10^2
FNO	c	1.16×10^{-2}	1.10×10^{-2}	2.33×10^{-2}	2.20×10^{-2}	4.24×10^{-2}	4.00×10^{-2}
	u	1.70×10^{-5}	1.00×10^0	6.50×10^{-5}	2.98×10^0	2.28×10^{-4}	1.13×10^0
	v	1.00×10^{-6}	4.50×10^{-1}	1.00×10^{-6}	1.28×10^0	1.00×10^{-6}	3.98×10^{-1}
	p	1.00×10^{-6}	1.38×10^2	1.00×10^{-6}	7.87×10^2	1.00×10^{-6}	2.69×10^2
CNO	c	1.74×10^{-2}	1.69×10^{-2}	1.72×10^{-2}	1.63×10^{-2}	3.78×10^{-2}	3.53×10^{-2}
	u	3.70×10^{-5}	1.51×10^0	3.60×10^{-5}	1.37×10^0	1.76×10^{-4}	1.74×10^0
	v	1.00×10^{-6}	6.87×10^{-1}	1.00×10^{-6}	6.85×10^{-1}	1.00×10^{-6}	5.98×10^{-1}
	p	1.00×10^{-6}	2.84×10^2	1.00×10^{-6}	2.93×10^2	1.00×10^{-6}	4.22×10^2
scOT	c	3.85×10^{-2}	3.69×10^{-2}	3.92×10^{-2}	3.79×10^{-2}	6.27×10^{-2}	6.09×10^{-2}
	u	1.73×10^{-4}	6.73×10^0	1.80×10^{-4}	5.73×10^0	4.85×10^{-4}	5.31×10^0
	v	3.00×10^{-6}	2.78×10^0	3.00×10^{-6}	2.12×10^0	2.00×10^{-6}	1.93×10^0
	p	3.00×10^{-6}	1.48×10^3	3.00×10^{-6}	1.34×10^3	4.00×10^{-6}	1.21×10^3
Poseidon	c	3.06×10^{-2}	2.84×10^{-2}	3.33×10^{-2}	3.17×10^{-2}	5.99×10^{-2}	5.79×10^{-1}
	u	1.01×10^{-4}	8.26×10^0	1.26×10^{-4}	6.49×10^0	4.30×10^{-4}	7.79×10^0
	v	5.00×10^{-6}	3.51×10^0	4.00×10^{-6}	2.47×10^0	5.00×10^{-6}	2.16×10^0
	p	5.00×10^{-6}	1.71×10^3	4.00×10^{-6}	1.48×10^3	5.00×10^{-6}	1.81×10^3

sharp interface dynamics compared to other models. Additionally, Figure 8 demonstrates that CNO is capable of capturing small bubble formation post-breakup, a key feature of multi-phase flow that is often difficult to learn with purely spectral or transformer-based architectures.

To complement our accuracy benchmarks, Table 7 reports the total number of trainable parameters for each model. While parameter count is a useful descriptor, we stress that enforcing equal parameter budgets across architectures -ranging from global Fourier operators (FNO), convolutional operators (CNO), deep MLP-based DeepONet, to attention-based transformers (scOT, Poseidon) - is both impractical and likely to obscure the inductive biases we wish to compare. For example, FNO’s spectral convolution mechanism operates fundamentally differently from the key-query-value projections of scOT/Poseidon, and CNO’s upsampling convolutions are not directly scalable to transformer-style attention layers. As theory and scaling laws show, each family achieves optimal performance on its own parameter scale (Wang and Wu, 2023). Thus, rather than artificially “equalizing” parameter counts, we compare each model in its best tuned form.

5 Conclusions

In summary, we have introduced a comprehensive time series dataset comprising 10,000 simulations in 2D and 1,000 simulations in 3D, focusing on bubble rise and droplet fall

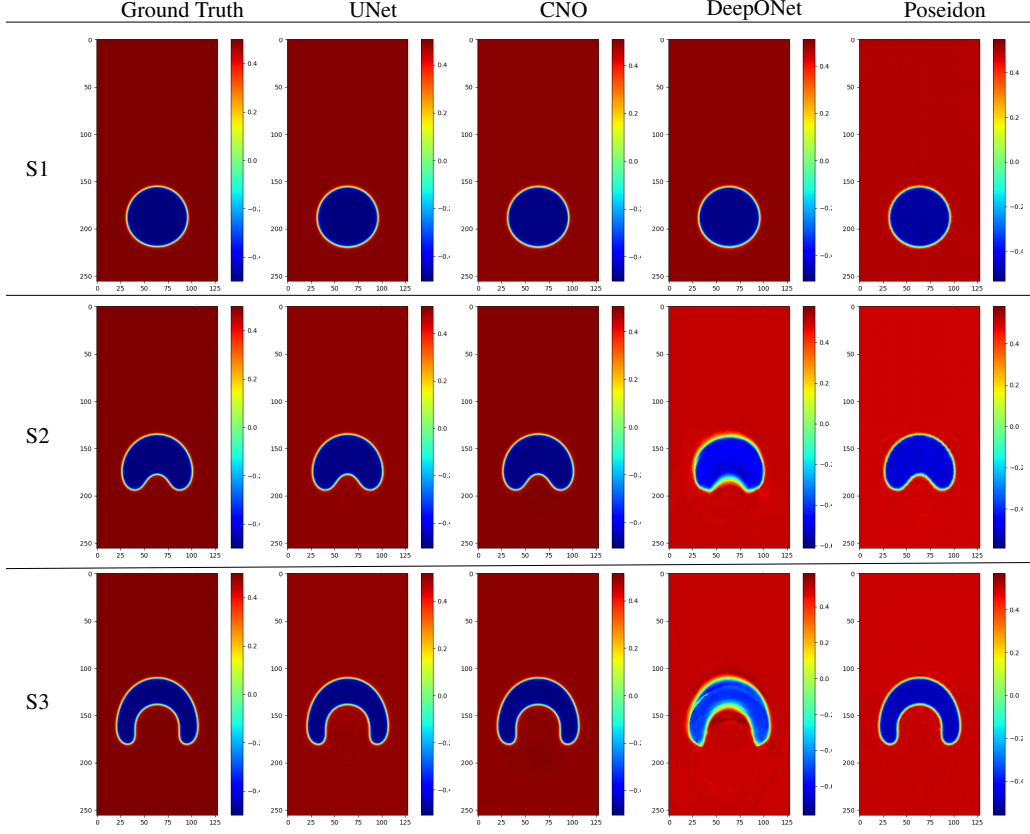


Figure 7: The figure presents a comparison of sequence-to-field predictions for the concentration field C against the ground truth. The predictions are generated by four models: UNet, Convolutional Neural Operator (CNO), DeepONet, and Poseidon, across three data subsets ($S1$, $S2$, and $S3$). Each row corresponds to a different subset ($S1$, $S2$, or $S3$), while each column displays the predictions made by the respective models.

Table 7: Total trainable parameter counts for each benchmarked model, showing different architectural paradigms operate at different parameters scales.

Model	params ($\times 10^6$)
UNet	7.7
DeepONet	0.9
FNO	10.9
CNO	11.7
scOT	20.7
Poseidon	20.7

dynamics. This dataset captures a wide range of two-phase flow phenomena, including simulations with density ratios as high as 1,000, Reynolds numbers up to 1,000, and Bond

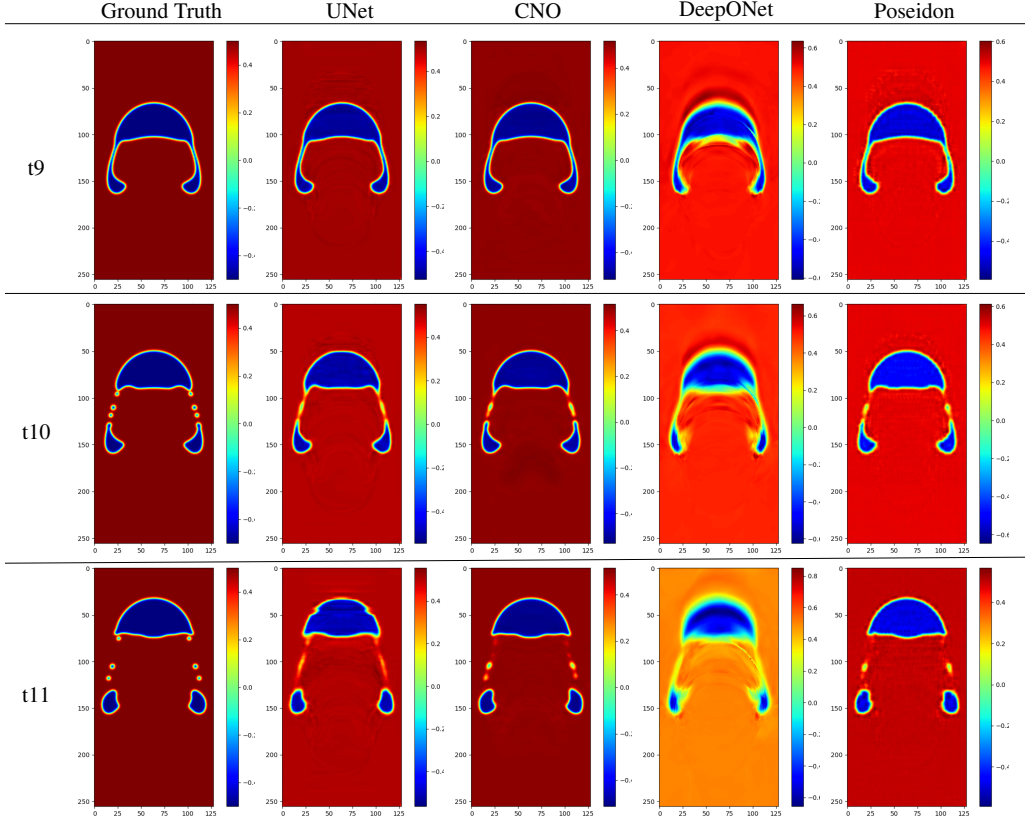


Figure 8: The figure presents sequence-to-sequence predictions for the concentration field C compared to the ground truth. Predictions are made by four models: UNet, Convolutional Neural Operator (CNO), DeepONet, and Poseidon. Each row represents different time steps (t_9 , t_{10} , and t_{11}) from dataset S_6 , while each column shows the predictions from the respective models.

numbers up to 500. Using a subsample of 1,000 samples from the bubble dataset, we successfully trained neural operators and foundation models, demonstrating encouraging results. By feeding in more time snapshots to models, they can more accurately predict the trajectory of bubble dynamics. Specifically, we found that CNO outperformed other models in capturing fine-scale interfacial details. We also concluded that the foundation model Poseidon pre-trained on single-phase phenomena might not be effective in learning multiphase flow, which demonstrates the need to train foundation models on multiphase flow data.

Generalizability and Applications: Models trained on MPFBench perform well on held-out test data, but real-world multiphase flows often deviate from those ideal conditions. For example, industrial meshes vary adaptively, and fluid properties may be non-Newtonian or temperature-dependent. Mitigation strategies include pretraining on more diverse multiphase data and applying physics constraints. Beyond benchmarking, MPFBench’s trained operators enable several practical uses. For example, the surrogate model can screen hundreds of channel geometries for droplet breakup or bubble coalescence much faster than CFD, thus

enhancing microfluidic design. Moreover, by providing reasonable initial guesses, neural operators can reduce costly solver iterations, thus accelerating the CFD workflow.

Limitations: The dataset has the following constraints:

- **Different orders of magnitude for solution fields:** The dataset includes solution fields that span different orders of magnitude. This is evident in the large disparity between the mean squared error (MSE) and relative L_2 errors for different solution fields.
- **Limited 3D Simulations:** Due to the substantial computational cost, only a small number of 3D simulations (1,000 cases) were conducted, resulting in a more restricted set of 3D cases in the dataset.
- **Model fitting with a limited number of time steps:** GPU memory limitations constrained the number of time steps that could be fitted on a single GPU. As a result, we had to use a limited number of time snapshots. An alternative approach could involve using an auto-regressive model to model the time series for each sample, inputting the predictions of previous time steps to predict the future time solutions to capture the full trajectory of the bubble.

Reproducibility Statement

In this work, we introduce a dataset and provide detailed explanations of the methodology and mathematical framework used for data generation in the Appendix [Section A](#). To evaluate the dataset, we applied various neural operators and foundation models, and the code for these models is available on our [GitHub](#) page. The repository includes detailed instructions for easy reproducibility of our results. All experiments were conducted on NVIDIA A100-SXM4 80GB. Please refer to the repository’s `README.md` for complete instructions on replicating the model evaluations.

CRedit authorship contribution statement

Mehdi Shadkhah: Conceptualization, Data curation, Formal Analysis, Investigation, Methodology, Software, Validation, Visualization, Writing – original draft, Writing – review & editing. **Ronak Tali:** Data curation, Formal Analysis, Software, Writing – original draft, Writing – review & editing. **Ali Rabeh:** Conceptualization, Data curation, Formal Analysis, Software, Writing – original draft, Writing – review & editing. **ChengHau Yang:** Visualization, Writing – original draft, Writing – review & editing. **Ethan Herron:** Software. **Abhisek Upadhyaya:** Software. **Adarsh Krishnamurthy:** Conceptualization, Validation, Writing – review & editing. **Chinmay Hegde:** Conceptualization. **Aditya Balu:** Conceptualization, Validation, Writing – review & editing. **Baskar Ganapathysubramanian:** Conceptualization, Funding acquisition, Project administration, Supervision, Writing – review & editing.

References

Ala S Al-Dogail and Rahul N Gajbhiye. Effects of density, viscosity and surface tension on flow regimes and pressure drop of two-phase flow in horizontal pipes. *Journal of Petroleum Science and Engineering*, 205:108719, 2021.

- Sebastian Aland and Axel Voigt. Benchmark computations of diffuse interface models for two-dimensional bubble dynamics. *International Journal for Numerical Methods in Fluids*, 69(3):747–761, 2012.
- Samuel M. Allen and John W. Cahn. Mechanisms of phase transformations within the miscibility gap of Fe-rich Fe-Al alloys. *Acta Metallurgica*, 24(5):425–437, may 1976. ISSN 00016160. doi: 10.1016/0001-6160(76)90063-8. URL <https://linkinghub.elsevier.com/retrieve/pii/0001616076900638>.
- Luz Amaya-Bower and Taehun Lee. Single bubble rising dynamics for moderate reynolds number using lattice boltzmann method. *Computers & Fluids*, 39(7):1191–1207, 2010. ISSN 0045-7930. doi: <https://doi.org/10.1016/j.compfluid.2010.03.003>. URL <https://www.sciencedirect.com/science/article/pii/S004579301000054X>.
- Shelley L Anna, Nathalie Bontoux, and Howard A Stone. Formation of dispersions using “flow focusing” in microchannels. *Applied physics letters*, 82(3):364–366, 2003.
- Utkarsh Ayachit. *The paraview guide: a parallel visualization application*. Kitware, Inc., 2015.
- D. Bhaga and M. E. Weber. Bubbles in viscous liquids: shapes, wakes and velocities. *Journal of Fluid Mechanics*, 105:61–85, 1981a. doi: 10.1017/S002211208100311X.
- D. Bhaga and M. E. Weber. Bubbles in viscous liquids: shapes, wakes and velocities. *Journal of Fluid Mechanics*, 105:61–85, 1981b. doi: 10.1017/S002211208100311X.
- Majdi Chaari, Abdennour C Seibi, Jalel Ben Hmida, and Afef Fekih. An optimized artificial neural network unifying model for steady-state liquid holdup estimation in two-phase gas–liquid flow. *Journal of Fluids Engineering*, 140(10):101301, 2018.
- Pao-Hsiung Chiu and Yan-Ting Lin. A conservative phase field method for solving incompressible two-phase flows. *Journal of Computational Physics*, 230(1):185–204, jan 2011. ISSN 00219991. doi: 10.1016/j.jcp.2010.09.021. URL <http://dx.doi.org/10.1016/j.jcp.2010.09.021><https://linkinghub.elsevier.com/retrieve/pii/S0021999110005243>.
- Carsten Cramer, Peter Fischer, and Erich J Windhab. Drop formation in a co-flowing ambient fluid. *Chemical Engineering Science*, 59(15):3045–3058, 2004.
- Hang Ding, Peter D.M. Spelt, and Chang Shu. Diffuse interface model for incompressible two-phase flows with large density ratios. *Journal of Computational Physics*, 226(2): 2078–2095, oct 2007. ISSN 00219991. doi: 10.1016/j.jcp.2007.06.028. URL <https://linkinghub.elsevier.com/retrieve/pii/S0021999107002793>.
- Jens Eggers and Emmanuel Villiermaux. Physics of liquid jets. *Reports on progress in physics*, 71(3):036601, 2008.
- Abbas Fakhari and Mohammad Hassan Rahimian. Investigation of deformation and breakup of a moving droplet by the method of lattice boltzmann equations. *International journal for numerical methods in fluids*, 64(8):827–849, 2010.

- Abbas Fakhari, Martin Geier, and Diogo Bolster. A simple phase-field model for interface tracking in three dimensions. *Computers & Mathematics with Applications*, 78(4):1154–1165, aug 2019. ISSN 08981221. doi: 10.1016/j.camwa.2016.08.021. URL <http://dx.doi.org/10.1016/j.camwa.2016.08.021><https://linkinghub.elsevier.com/retrieve/pii/S0898122116304758>.
- Martin Geier, Abbas Fakhari, and Taehun Lee. Conservative phase-field lattice Boltzmann model for interface tracking equation. *Physical Review E*, 91(6):063309, jun 2015. ISSN 1539-3755. doi: 10.1103/PhysRevE.91.063309. URL <https://link.aps.org/doi/10.1103/PhysRevE.91.063309>.
- Monica Gumulya, Jyeshtharaj B. Joshi, Ranjeet P. Utikar, Geoffrey M. Evans, and Vishnu Pareek. Bubbles in viscous liquids: Time dependent behaviour and wake characteristics. *Chemical Engineering Science*, 144:298–309, 2016. ISSN 0009-2509. doi: <https://doi.org/10.1016/j.ces.2016.01.051>. URL <https://www.sciencedirect.com/science/article/pii/S0009250916300318>.
- Zhaoli Guo, Chuguang Zheng, and Baochang Shi. Discrete lattice effects on the forcing term in the lattice Boltzmann method. *Physical Review E*, 65(4):046308, apr 2002. ISSN 1063-651X. doi: 10.1103/PhysRevE.65.046308. URL <https://link.aps.org/doi/10.1103/PhysRevE.65.046308>.
- Stefan Haeberle and Roland Zengerle. Microfluidic platforms for lab-on-a-chip applications. *Lab on a Chip*, 7(9):1094–1110, 2007.
- Sheikh Md Shakeel Hassan, Arthur Feeney, Akash Dhruv, Jihoon Kim, Youngjoon Suh, Jaiyoung Ryu, Yoonjin Won, and Aparna Chandramowlishwaran. BubbleML: A multiphase multiphysics dataset and benchmarks for machine learning. In *Thirty-seventh Conference on Neural Information Processing Systems Datasets and Benchmarks Track*, 2023. URL <https://openreview.net/forum?id=0Wmglu8zak>.
- Maximilian Herde, Bogdan Raonić, Tobias Rohner, Roger Käppeli, Roberto Molinaro, Emmanuel de Bézenac, and Siddhartha Mishra. Poseidon: Efficient foundation models for pdes, 2024.
- Sophie Hernot and Alexander L Klibanov. Microbubbles in ultrasound-triggered drug and gene delivery. *Advanced drug delivery reviews*, 60(10):1153–1166, 2008.
- Jinsong Hua and Jing Lou. Numerical simulation of bubble rising in viscous liquid. *Journal of Computational Physics*, 222(2):769–795, 2007. ISSN 0021-9991. doi: <https://doi.org/10.1016/j.jcp.2006.08.008>. URL <https://www.sciencedirect.com/science/article/pii/S0021999106003949>.
- Haibo Huang, Michael C. Sukop, and Xi Yun Lu. *Multiphase Lattice Boltzmann Methods: Theory and Application*. John Wiley & Sons, Ltd, jul 2015. ISBN 9781118971338. doi: 10.1002/9781118971451. URL <http://doi.wiley.com/10.1002/9781118971451>.
- Shu-Ren Hysing, Stefan Turek, Dmitri Kuzmin, Nicola Parolini, Erik Burman, Sashikumaar Ganesan, and Lutz Tobiska. Quantitative benchmark computations of two-dimensional

- bubble dynamics. *International Journal for Numerical Methods in Fluids*, 60(11):1259–1288, 2009.
- David Jacqmin. Calculation of Two-Phase Navier-Stokes Flows Using Phase-Field Modeling. *Journal of Computational Physics*, 155(1):96–127, oct 1999. ISSN 00219991. doi: 10.1006/jcph.1999.6332. URL <https://linkinghub.elsevier.com/retrieve/pii/S0021999199963325>.
- DAVID JACQMIN. Contact-line dynamics of a diffuse fluid interface. *Journal of Fluid Mechanics*, 402:57–88, jan 2000. ISSN 0022-1120. doi: 10.1017/S0022112099006874. URL https://www.cambridge.org/core/product/identifier/S0022112099006874/type/journal_article.
- M. Jalaal and K. Mehravaran. Fragmentation of falling liquid droplets in bag breakup mode. *International Journal of Multiphase Flow*, 47:115–132, 2012. ISSN 0301-9322. doi: <https://doi.org/10.1016/j.ijmultiphaseflow.2012.07.011>. URL <https://www.sciencedirect.com/science/article/pii/S0301932212001140>.
- Didier Jamet, David Torres, and J. U. Brackbill. On the theory and computation of surface tension: The elimination of parasitic currents through energy conservation in the second-gradient method. *Journal of Computational Physics*, 182(1):262–276, oct 2002. ISSN 00219991. doi: 10.1006/jcph.2002.7165.
- George Em Karniadakis, Ioannis G. Kevrekidis, Lu Lu, Paris Perdikaris, Sifan Wang, and Liu Yang. Physics-informed machine learning. *Nature Reviews Physics*, 3(6):422–440, 2021. ISSN 25225820. doi: 10.1038/s42254-021-00314-5. URL <https://doi.org/10.1038/s42254-021-00314-5>.
- Makrand A. Khanwale, Kumar Saurabh, Masado Ishii, Hari Sundar, James A. Rossmannith, and Baskar Ganapathysubramanian. A projection-based, semi-implicit time-stepping approach for the cahn-hilliard navier-stokes equations on adaptive octree meshes. *Journal of Computational Physics*, 475:111874, 2023. ISSN 0021-9991. doi: <https://doi.org/10.1016/j.jcp.2022.111874>. URL <https://www.sciencedirect.com/science/article/pii/S0021999122009378>.
- Timm Krüger, Halim Kusumaatmaja, Alexandr Kuzmin, Orest Shardt, Goncalo Silva, and Erlend Magnus Viggen. *The Lattice Boltzmann Method*, volume 58 of *Graduate Texts in Physics*. Springer International Publishing, 2017. ISBN 978-3-319-44647-9. doi: 10.1007/978-3-319-44649-3. URL <http://link.springer.com/10.1007/978-3-319-44649-3>.
- Q. Li, K. H. Luo, Y. J. Gao, and Y. L. He. Additional interfacial force in lattice Boltzmann models for incompressible multiphase flows. *Physical Review E*, 85(2):026704, feb 2012. ISSN 1539-3755. doi: 10.1103/PhysRevE.85.026704. URL <https://link.aps.org/doi/10.1103/PhysRevE.85.026704>.
- Zijie Li, Dule Shu, and Amir Barati Farimani. Scalable transformer for pde surrogate modeling. In A. Oh, T. Naumann, A. Globerson, K. Saenko, M. Hardt, and S. Levine, editors, *Advances in Neural Information Processing Systems*, volume 36, pages 28010–28039.

- Curran Associates, Inc., 2023. URL https://proceedings.neurips.cc/paper_files/paper/2023/file/590daf74f99ee85df3d8c007df9c8187-Paper-Conference.pdf.
- Zongyi Li, Nikola Kovachki, Kamyar Azizzadenesheli, Burigede Liu, Kaushik Bhattacharya, Andrew Stuart, and Anima Anandkumar. Fourier neural operator for parametric partial differential equations, 2021.
- Chensen Lin, Zhen Li, Lu Lu, Shengze Cai, Martin Maxey, and George Em Karniadakis. Operator learning for predicting multiscale bubble growth dynamics. *The Journal of Chemical Physics*, 154(10), 2021a.
- Chensen Lin, Martin Maxey, Zhen Li, and George Em Karniadakis. A seamless multiscale operator neural network for inferring bubble dynamics. *Journal of Fluid Mechanics*, 929: A18, 2021b.
- Zhaomiao Liu, Fanming Cai, Yan Pang, Yanlin Ren, Nan Zheng, Rui Chen, and Siyu Zhao. Enhanced droplet formation in a t-junction microchannel using electric field: A lattice boltzmann study. *Physics of Fluids*, 34(8), 2022.
- Lu Lu, Pengzhan Jin, Guofei Pang, Zhongqiang Zhang, and George Em Karniadakis. Learning nonlinear operators via deepnet based on the universal approximation theorem of operators. *Nature Machine Intelligence*, 3:218–229, 2021.
- Rômulo M Silva, Malú Grave, and Alvaro LGA Coutinho. A pinn-based level-set formulation for reconstruction of bubble dynamics. *Archive of Applied Mechanics*, pages 1–16, 2024.
- Daniel Mark, Stefan Haeberle, Günter Roth, Felix Von Stetten, and Roland Zengerle. Microfluidic lab-on-a-chip platforms: requirements, characteristics and applications. *Microfluidics based microsystems: fundamentals and applications*, pages 305–376, 2010.
- Oliver Penrose and Paul C. Fife. Thermodynamically consistent models of phase-field type for the kinetic of phase transitions. *Physica D: Nonlinear Phenomena*, 43(1): 44–62, may 1990. ISSN 01672789. doi: 10.1016/0167-2789(90)90015-H. URL <https://linkinghub.elsevier.com/retrieve/pii/016727899090015H>.
- Andrea Prosperetti. Motion of two superposed viscous fluids. *Physics of Fluids*, 24(7): 1217 – 1223, 1981. doi: 10.1063/1.863522. URL <https://www.scopus.com/inward/record.uri?eid=2-s2.0-0019376759&doi=10.1063%2f1.863522&partnerID=40&md5=eb53d8f4f5117a9f1224ba3ed1d61239>. Cited by: 149.
- Ali Rabeh, Ethan Herron, Aditya Balu, Soumik Sarkar, Chinmay Hegde, Adarsh Krishnamurthy, and Baskar Ganapathysubramanian. Geometry matters: Benchmarking scientific ml approaches for flow prediction around complex geometries. *arXiv preprint arXiv:2501.01453*, 2024a.
- Ali Rabeh, Makrand A Khanwale, John J Lee, and Baskar Ganapathysubramanian. Modeling and simulations of high-density two-phase flows using projection-based cahn-hilliard navier-stokes equations. *arXiv preprint arXiv:2406.17933*, 2024b.

- Maziar Raissi, Paris Perdikaris, and George E Karniadakis. Physics-informed neural networks: A deep learning framework for solving forward and inverse problems involving nonlinear partial differential equations. *Journal of Computational physics*, 378:686–707, 2019.
- Bogdan Raonić, Roberto Molinaro, Tim De Ryck, Tobias Rohner, Francesca Bartolucci, Rima Alaifari, Siddhartha Mishra, and Emmanuel de Bézenac. Convolutional neural operators for robust and accurate learning of pdes, 2023.
- Pratik Rathore, Weimu Lei, Zachary Frangella, Lu Lu, and Madeleine Udell. Challenges in training pinns: A loss landscape perspective. *arXiv preprint arXiv:2402.01868*, 2024.
- Feng Ren, Baowei Song, Michael C. Sukop, and Haibao Hu. Improved lattice boltzmann modeling of binary flow based on the conservative allen-cahn equation. *Phys. Rev. E*, 94:023311, Aug 2016. doi: 10.1103/PhysRevE.94.023311. URL <https://link.aps.org/doi/10.1103/PhysRevE.94.023311>.
- Olaf Ronneberger, Philipp Fischer, and Thomas Brox. U-net: Convolutional networks for biomedical image segmentation. In *Medical image computing and computer-assisted intervention—MICCAI 2015: 18th international conference, Munich, Germany, October 5–9, 2015, proceedings, part III 18*, pages 234–241. Springer, 2015.
- Alvaro Sanchez-Gonzalez, Jonathan Godwin, Tobias Pfaff, Rex Ying, Jure Leskovec, and Peter Battaglia. Learning to simulate complex physics with graph networks. In *International conference on machine learning*, pages 8459–8468. PMLR, 2020.
- Amirmohammad Sattari, Pedram Hanafizadeh, and Mina Hoorfar. Multiphase flow in microfluidics: From droplets and bubbles to the encapsulated structures. *Advances in Colloid and Interface Science*, 282:102208, 2020.
- Norbert Schwesinger, Thomas Frank, and Helmut Wurmus. A modular microfluid system with an integrated micromixer. *Journal of Micromechanics and Microengineering*, 6(1):99, 1996.
- Drue Seksinsky and Jeffrey S Marshall. Droplet impingement on a surface at low reynolds numbers. *Journal of Fluids Engineering*, 143(2):021304, 2021.
- Mehdi Shadkhah, Mohammad Taeibi Rahni, Azadeh Kebriaee, and Mohammad Reza Salimi. Clip: A cuda-accelerated lattice boltzmann framework for interfacial phenomena with application to liquid jet simulations, 2025. URL <https://arxiv.org/abs/2505.12205>.
- Satyvir Singh. Role of atwood number on flow morphology of a planar shock-accelerated square bubble: A numerical study. *Physics of Fluids*, 32(12), 2020.
- Abraham D Stroock, Stephan KW Dertinger, Armand Ajdari, Igor Mezic, Howard A Stone, and George M Whitesides. Chaotic mixer for microchannels. *Science*, 295(5555):647–651, 2002.
- Michael C. Sukop and Daniel T. Thorne. *Lattice boltzmann modeling: An introduction for geoscientists and engineers*. Springer Berlin Heidelberg, 2006. ISBN 3540279814. doi: 10.1007/978-3-540-27982-2. URL <http://link.springer.com/10.1007/978-3-540-27982-2>.

- Ronak Tali, Ali Rabeh, Cheng-Hau Yang, Mehdi Shadkhah, Samundra Karki, Abhisek Upadhyaya, Suriya Dhakshinamoorthy, Marjan Saadati, Soumik Sarkar, Adarsh Krishnamurthy, et al. Flowbench: A large scale benchmark for flow simulation over complex geometries. *arXiv preprint arXiv:2409.18032*, 2024.
- Todd Thorsen, Richard W Roberts, Frances H Arnold, and Stephen R Quake. Dynamic pattern formation in a vesicle-generating microfluidic device. *Physical review letters*, 86(18):4163, 2001.
- Joshua D Tice, Helen Song, Adam D Lyon, and Rustem F Ismagilov. Formation of droplets and mixing in multiphase microfluidics at low values of the reynolds and the capillary numbers. *Langmuir*, 19(22):9127–9133, 2003.
- Anja Vananroye, Pieter JA Janssen, Patrick D Anderson, Peter Van Puyvelde, and Paula Moldenaers. Microconfined equiviscous droplet deformation: Comparison of experimental and numerical results. *Physics of Fluids*, 20(1), 2008.
- Konstantinos Vontas, Cristina Boscariol, Manolia Andredaki, Anastasios Georgoulas, Cyril Crua, Jens Honoré Walther, and Marco Marengo. Droplet impact on suspended metallic meshes: Effects of wettability, reynolds and weber numbers. *Fluids*, 5(2):81, 2020.
- Zihao Wang and Lei Wu. Theoretical analysis of the inductive biases in deep convolutional networks. *Advances in Neural Information Processing Systems*, 36:74289–74338, 2023.
- Zhikun Xu, Tianyou Wang, and Zhizhao Che. Droplet deformation and breakup in shear flow of air. *Physics of Fluids*, 32(5), 2020.
- Y. Y. Yan and Y. Q. Zu. A lattice Boltzmann method for incompressible two-phase flows on partial wetting surface with large density ratio. *Journal of Computational Physics*, 227(1):763–775, nov 2007. ISSN 10902716. doi: 10.1016/j.jcp.2007.08.010. URL <https://linkinghub.elsevier.com/retrieve/pii/S0021999107003580>.
- Junxiang Yang, Darae Jeong, and Junseok Kim. A fast and practical adaptive finite difference method for the conservative allen–cahn model in two-phase flow system. *International Journal of Multiphase Flow*, 137:103561, 2021. ISSN 0301-9322. doi: <https://doi.org/10.1016/j.ijmultiphaseflow.2021.103561>. URL <https://www.sciencedirect.com/science/article/pii/S0301932221000094>.
- H. Z. Yuan, Z. Chen, C. Shu, Y. Wang, X. D. Niu, and S. Shu. A free energy-based surface tension force model for simulation of multiphase flows by level-set method. *Journal of Computational Physics*, 345:404–426, 2017. ISSN 10902716. doi: 10.1016/j.jcp.2017.05.020.
- Y. Q. Zu and S. He. Phase-field-based lattice boltzmann model for incompressible binary fluid systems with density and viscosity contrasts. *Phys. Rev. E*, 87:043301, Apr 2013. doi: 10.1103/PhysRevE.87.043301. URL <https://link.aps.org/doi/10.1103/PhysRevE.87.043301>.

Appendix A. Details of the CFD simulation framework

Our computational framework employs the CUDA platform to implement the algorithms necessary for the Lattice Boltzmann Method (LBM). We achieve significant computational performance enhancements by leveraging CUDA's parallel processing capabilities. The primary performance bottleneck in GPU architectures is often the data transfer between GPU memory and unified CPU memory. To mitigate this, we minimize such data transfers, conducting them only when necessary for convergence checks or final output retrieval.

We utilize a single one-dimensional array in conjunction with macro functions to handle the substantial data volumes intrinsic to LBM simulations. This method optimizes memory usage and computational efficiency on the GPU, ensuring that we fully exploit the GPU's computational power and memory bandwidth. This strategy allows for the high-performance execution of LBM algorithms, crucial for large-scale simulations and complex fluid dynamics problems.

A.1 Formulation of Navier-Stokes and Allen-Cahn equations

Several lattice Boltzmann models, such as the Cahn-Hilliard and Allen-Cahn models, utilize interface tracking equations and are thus categorized as phase-field models (Penrose and Fife, 1990; Jacqmin, 1999). These models describe multiphase flows using a diffuse interface, with the Allen-Cahn equation commonly employed for this purpose (Allen and Cahn, 1976). In some studies, this approach is called the conservative phase-field LB model (Fakhari et al., 2019). The phase-field variable, ϕ , which tracks the interface, ranges from 0 to 1, leading to the following expression for the phase-field equation (Chiu and Lin, 2011):

$$\frac{\partial \phi}{\partial t} + \nabla \cdot (\phi u) = \nabla \cdot \left[M \left(\nabla \phi - \frac{1 - 4(\phi - \phi_0)^2}{\xi} \hat{n} \right) \right], \quad (2)$$

where t represents time, u is the velocity, M denotes a positive constant for the mobility parameter, ξ is the interfacial thickness, and $\phi_0 = \frac{\phi_H + \phi_L}{2}$. ϕ_H and ϕ_L represent the interface indicator values for the heavy and light fluids, respectively, set to 1.0 for the heavy fluid and 0.0 for the light fluid. The unit normal vector \hat{n} for the interface can be defined as:

$$\hat{n} = \frac{\nabla \phi}{|\nabla \phi|}. \quad (3)$$

Note, the interface location at x_0 is initialized as (Yan and Zu, 2007):

$$\phi(x) = \phi_0 \pm \frac{\phi_H - \phi_L}{2} \tanh\left(\frac{|x - x_0|}{\xi/2}\right). \quad (4)$$

According to the phase-field model, the following equations exist for incompressible multiphase flows (Ding et al., 2007; Li et al., 2012):

$$\frac{\partial \rho}{\partial t} + \nabla \cdot (\rho u) = 0, \quad (5a)$$

$$\rho \left(\frac{\partial u}{\partial t} + u \cdot \nabla u \right) = -\nabla p + \nabla \cdot (\mu [\nabla u + (\nabla u)^T]) + F_s + F_b. \quad (5b)$$

In Equation 5a, ρ represents the density of fluids, p denotes the macroscopic pressure, F_b is the body force, and F_s corresponds to the surface tension force. The equation for calculating the surface tension force term is also expressed as (Jamet et al., 2002):

$$F_s = \mu_\phi \nabla \phi, \quad (6)$$

where

$$\mu_\phi = 4\beta\phi(\phi - 1)(\phi - 1/2) - \kappa\nabla^2\phi, \quad (7)$$

denotes the chemical potential equation utilized for binary fluids (JACQMIN, 2000). Equation 8 establishes a relation between the coefficients β and κ , interface thickness ξ , and surface tension σ , as;

$$\beta = 12\sigma/\xi, \quad \kappa = 3\sigma\xi/2. \quad (8)$$

A.2 Lattice Boltzmann Method

Given that interfaces are typically of mesoscopic scale, the kinetic-based Lattice Boltzmann Method (LBM) presents a more effective approach for simulating multiphase flows compared to traditional Navier-Stokes solvers (Sukop and Thorne, 2006; Huang et al., 2015). The Chapman-Enskog analysis validates the consistency between the LBM and the Navier-Stokes equations (Krüger et al., 2017). In this study, we investigate hydrodynamic properties such as velocity and pressure using the standard form of the Lattice Boltzmann equation as outlined in (Guo et al., 2002):

$$f_a(x + e_a\delta t, t + \delta t) = f_a(x, t) + \Omega_a(x, t) + F_a(x, t), \quad (9)$$

In this context, f_a denotes the velocity-based hydrodynamic distribution function for incompressible fluids, Ω_a represents the collision operator, and F_a signifies the force term. This study employs the two-dimensional nine-velocity (D2Q9) model for 2D simulations and the three-dimensional nineteen-velocity (D3Q19) model for 3D simulations.

To define the interface between phases, we employed the following Lattice Boltzmann Equation (LBE) to accurately determine the interface between fluid phases (Geier et al., 2015):

$$g_a(x + e_a\delta t, t + \delta t) = g_a(x, t) - \frac{g_a(x, t) - \bar{g}_a^{eq}(x, t)}{\tau_\phi + 1/2} + F_a^\phi(x, t). \quad (10)$$

Here, g_a represents the distribution function for the phase-field, and τ_ϕ denotes the dimensionless phase-field relaxation time. The forcing term is calculated as follows:

$$F_a^\phi(x, t) = \delta t \frac{[1 - 4(\phi - \phi_0)^2]}{\xi} \omega_a e_a \cdot \frac{\nabla \phi}{|\nabla \phi|}. \quad (11)$$

In Equation 11, ω_a and e_a denote the weight coefficient and the mesoscopic velocity set, respectively. Here, ξ denotes the thickness of the interface. As illustrated in Figure 9, we carefully selected this parameter to ensure adequate lattice nodes within the interface.

This choice is critical for accurately capturing the complex physics in the rapid change of material properties across the interface. The appropriate selection of ξ ensures that the computational mesh can effectively represent the gradients and variations within the interface, thus enhancing the overall stability and accuracy of the simulation.

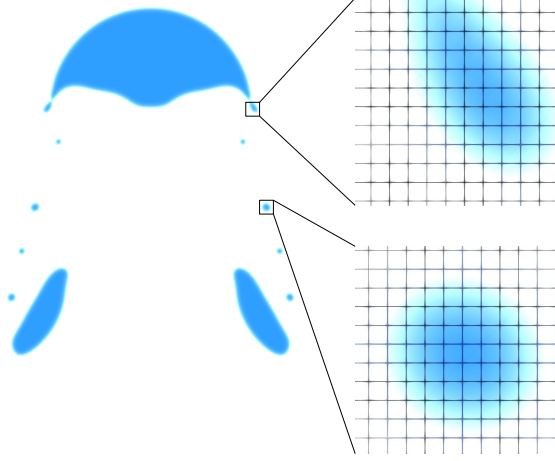


Figure 9: *Illustration of the interface region captured by the computational mesh. The magnified views show the distribution of lattice nodes within the interface, ensuring precise resolution of interfacial dynamics and transitions. The careful selection of the interface thickness parameter ξ ensures that the mesh adequately represents the gradients and variations in the interface region.*

A.3 Validation

In this section, we validate our numerical model through benchmark tests covering a range of two-phase flow phenomena. We include four distinct validation cases to comprehensively assess the accuracy and robustness of our approach: (1) the capillary wave problem, which evaluates the model’s capability to handle surface tension-driven flows; (2) the bubble rising dynamics, which tests the interaction between buoyancy and viscous forces; (3) the falling droplet dynamics, which examines the breakup mechanisms of liquid droplets under gravity; and (4) the Rayleigh-Taylor instability, which explores the interfacial instability between fluids of differing densities under gravitational influence. Each subsection compares our simulation results and established experimental or numerical data, demonstrating the model’s fidelity across various flow regimes.

A.3.1 CAPILLARY WAVE

To validate our Lattice Boltzmann Method (LBM) simulations of two-phase flow, we focus on the dynamic behavior of capillary waves at the interface between two immiscible fluids. In our study, a sinusoidal perturbation with a small amplitude η_0 and wave number k is applied to the initially quiescent interface. This setup provides a rigorous test for the LBM framework, as it has a well-established analytical solution for cases with identical kinematic viscosities ν but differing densities of the two fluids. The temporal evolution of the interface

amplitude $\eta(t)$ is utilized as a benchmark for our simulations. The analytical expression for the decay of the wave amplitude, $\eta(t)$, is given by (Prosperetti, 1981):

$$\frac{\eta(t)}{\eta_0} = \frac{4(1-4\gamma)\nu^2 k^4}{8(1-4\gamma)\nu^2 k^4 + \omega_0} \operatorname{erfc}(\sqrt{\nu k^2 t}) + \sum_{i=1}^4 \frac{z_i}{Z_i} \frac{\omega_0^2}{z_i^2 - \nu k^2} e^{(z_i^2 - \nu k^2)t} \operatorname{erfc}(z_i \sqrt{\nu t}) \quad (12)$$

where $\omega_0 = \sqrt{\frac{\sigma k^3}{\rho_H + \rho_L}}$ is the angular frequency, $\gamma = \frac{\rho_H \rho_L}{(\rho_H + \rho_L)^2}$ and $Z_i = \prod_{\substack{1 \leq j \leq 4 \\ j \neq i}} (z_j - z_i)$.

The evaluation of the complementary error function $\operatorname{erfc}(z_i)$ can be done by solving the following algebraic equation:

$$z^4 - 4\gamma\sqrt{\nu k^2} z^3 + 2(1-6\gamma)\nu k^2 z^2 + 4(1-3\gamma)(\nu k^2)^{3/2} z + (1-4\gamma)\nu k^2 + \omega_0^2 = 0. \quad (13)$$

Our validation involves analyzing the propagation of capillary waves, an inherently transient process that tests the model's ability to accurately capture key physical parameters such as density and viscosity ratios, along with surface tension effects. By varying these parameters and the wavelength, we compare the simulation results with predictions from linear theory. According to Figure 10, the lighter fluid with density ρ_L overlays the heavier fluid with density ρ_H , with the initial interface described by $y = L + \eta_0 \cos(2\pi x)$, where η_0 is the initial perturbation amplitude. The decay of this wavy profile to a flat interface, driven by viscosity and surface tension, without external forces like gravity, serves as a critical validation test for our LBM approach. The computational domain is discretized

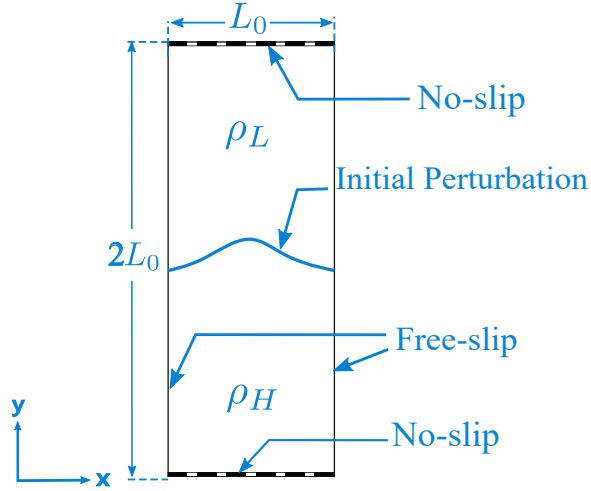


Figure 10: Schematic diagram of the capillary wave problem setup.

into a grid of 256 by 512 lattice nodes. Free-slip boundary conditions are applied in the direction of wave propagation, while no-slip conditions are imposed at the top and bottom boundaries. The simulation parameters are set as follows: $\eta_0 = 0.02$, $\sigma = 10^{-4}$, $\xi = 4$, and $M_\phi = 0.02$. Since the interface may not align exactly with the grid points, the values of $\eta(t)$ are interpolated from ϕ values using the following relationship:

$$\eta(t) = y - \frac{\phi(x_{L_0/2}, y)}{\phi(x_{L_0/2}, y) - \phi(x_{L_0/2}, y-1)}, \quad \phi(x_{L_0/2}, y)\phi(x_{L_0/2}, y-1) < 0. \quad (14)$$

The length (η) and time scales (t) are normalized by the initial amplitude a_0 and the angular frequency ω_0 , respectively, denoted as $\eta^* = \eta/\eta_0$ and $t^* = t\omega_0$.

It is worth noting that angular frequency is crucial for any wave system. It depends on surface tension, viscosity, wave number, and density values. The equation is derived assuming that both fluids have the same viscosity, set to $\nu = 0.005, 0.0005$. Note that the wavelength magnitude matches the grid size $L_0 = 256$.

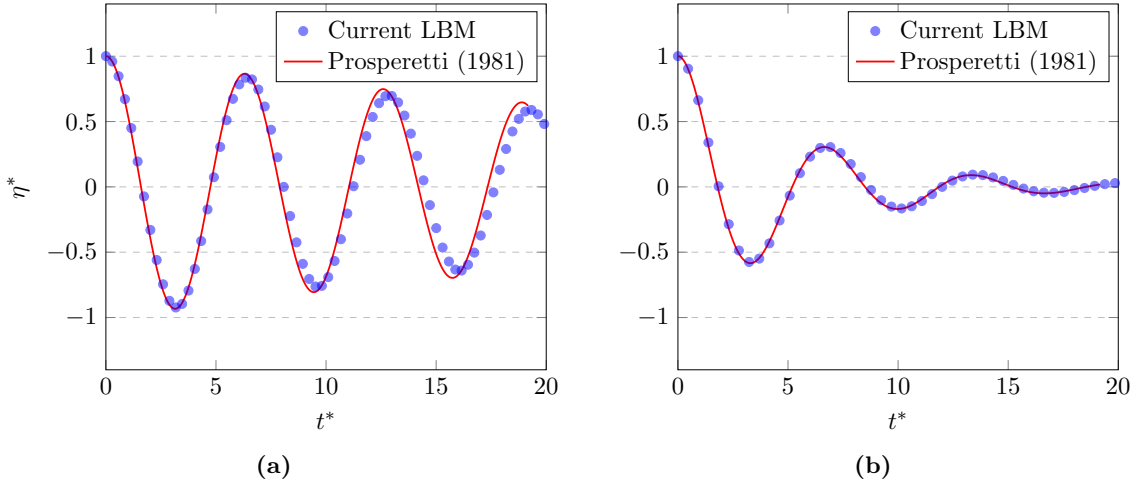


Figure 11: Comparison of the normalized interface amplitude η^* as a function of normalized time t^* between the current LBM simulation and the analytical solution by Prosperetti (1981). (a) corresponds to a viscosity of $\nu = 0.0005$, and (b) corresponds to a viscosity of $\nu = 0.005$. The LBM results (blue circles) closely match the analytical results (red line).

A.3.2 RISE OF A SINGLE BUBBLE IN QUIESCENT FLUID

The dynamics of a rising bubble have been extensively studied due to their significance in various natural and industrial processes. When a bubble rises through a liquid, it is subjected to several forces, including buoyancy, drag, and surface tension, which influences its shape, velocity, and trajectory (Bhaga and Weber, 1981b; Amaya-Bower and Lee, 2010; Hua and Lou, 2007; Khanwale et al., 2023). Our investigation focuses on the dynamics of a bubble rising within a rectangular channel. The simulation begins with a circular bubble of diameter $D = L_0/5$ placed at the coordinates $(L_0/2, L_0/2)$ within a domain with a length of L_0 and a height of $4L_0$. Boundary conditions are set such that the no-slip is applied at the top and bottom, while free-slip boundary conditions are used for the lateral boundaries. The fluids experience a volumetric buoyancy force $F_b = -(\rho - \rho_h)g_y\mathbf{j}$, where g_y represents the gravitational acceleration in the y -direction. This study highlights four crucial dimensionless parameters: the density ratio ρ_h/ρ_l , the viscosity ratio μ_h/μ_l , the gravity Reynolds number, and the Eötvös (Bond) number.

The gravity Reynolds number is defined as:

$$\text{Re}_h = \frac{\sqrt{g_y \rho_h (\rho_h - \rho_l) D^3}}{\mu_h} \quad (15)$$

The Eötvös (Bond) number is defined as:

$$\text{Eo} = \frac{g_y (\rho_h - \rho_l) D^2}{\sigma} \quad (16)$$

In many studies, the Morton number is also considered, defined as:

$$\text{Mo} = \frac{g_y (\rho_h - \rho_l) \mu_h^4}{\sigma^3 \rho_h^2} \quad (17)$$

The dimensionless time is also defined by:

$$t^* = t \sqrt{\frac{g_y}{D}} \quad (18)$$

The reference velocity scale needed in the Péclet number can be chosen for gravity-driven flows as $U_0 = \sqrt{g_y D}$. Four sets of simulations are conducted at Four different Eötvös and Morton numbers. The density and viscosity ratios are fixed at 1,000 and 100, respectively. The numerical parameters are $L_0 = 512$, $\text{Pe} = 25$ and $\text{Cn} = 0.010$, and the LBM simulation results are shown in [Figure 12](#).

To evaluate the accuracy and reliability of the proposed LBM, a comparison is made between the results obtained from the LBM approach and those from the experiments and FVM, as illustrated in [Figure 12](#). In the spherical regime, surface tension dominates, resulting in small bubbles that maintain a nearly spherical shape due to the strong cohesive forces at the interface. As the bubble size increases, the shape transitions to an ellipsoidal form. In this ellipsoidal regime, the inertial forces become more significant, causing the bubble to deform. This deformation is influenced by the surrounding liquid's viscosity and the interface's surface tension. The dynamics of this regime can be described using correlations that account for the balance between inertial and surface tension forces (Amaya-Bower and Lee, 2010). In the spherical cap regime, the bubbles are large enough that inertia forces dominate, leading to further deformation into a cap shape. This regime is characterized by a significant increase in terminal velocity, which is proportional to the size of the bubble (Bhaga and Weber, 1981a). These patterns are consistent among all results.

A.3.3 FALLING DROPLET

The dynamics of a falling droplet under gravity is another fascinating two-phase flow phenomenon that has been extensively studied in the literature (Yang et al., 2021; Jalaal and Mehravaran, 2012). In this study, a liquid droplet with diameter $D = L_0/5$ is initially placed at $(L_0/2, 6L_0/2)$ within a rectangular computational domain of length L_0 and height $3L_0$. The same boundary conditions are applied as in the bubble rising simulations: the no-slip boundary condition is applied at the top and bottom, while free-slip boundary conditions are imposed at the lateral boundaries. The volumetric buoyancy force $F_b = -(\rho - \rho_l)g_y \mathbf{j}$,

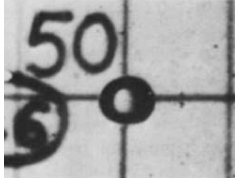
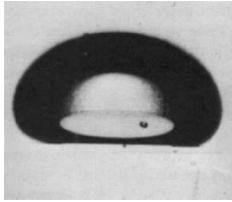
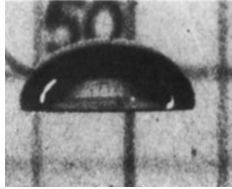

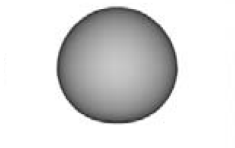


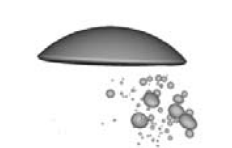
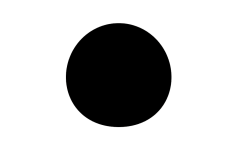



	A1 $Bo = 17.7$ $Mo = 711$	A2 $Bo = 243$ $Mo = 266$	A3 $Bo = 115$ $Mo = 1.31$	A4 $Bo = 115$ $Mo = 0.001$
Experiment				
FVM (3D)				
LBM (2D)				

Figure 12: Comparison of bubble shapes at constant rise velocity: Experimental results by (Bhaga and Weber, 1981a), LBM results, and FVM results by (Gumulya et al., 2016) for various Bond numbers (Bo) and Morton numbers (Mo).

where \mathbf{j} is unit vector in y -direction and g_y represents the gravitational acceleration in the y -direction, acts on the fluids.

The dimensionless analysis identifies several key parameters that characterize the flow: the density ratio ρ_h/ρ_l , the viscosity ratio μ_h/μ_l , the gravity Reynolds number, and the Eötvös (Bond) number. The gravity Reynolds number is defined as:

$$Re_h = \frac{\sqrt{g_y \rho_h (\rho_h - \rho_l) D^3}}{\mu_h} \quad (19)$$

Similarly, the Eötvös number, which represents the ratio of gravitational forces to surface tension forces, is given by:

$$Eo = \frac{g_y (\rho_h - \rho_l) D^2}{\sigma} \quad (20)$$

Another important dimensionless group in the literature is the Morton number, which characterizes the fluid properties affecting the bubble and droplet dynamics:

$$Mo = \frac{g_y (\rho_h - \rho_l) \mu_h^4}{\sigma^3 \rho_h^2} \quad (21)$$

The Ohnesorge number (Oh) is a dimensionless number that characterizes the relative importance of viscous forces compared to inertial and surface tension forces in a fluid. It is particularly relevant in the study of droplet dynamics and is defined as:

$$\text{Oh} = \frac{\mu_h}{\sqrt{\rho_h \sigma D}} \quad (22)$$

The simulation is conducted at a moderate density ratio to capture the breakup mechanisms of the falling droplet, allowing for comparisons with the VOF model. The simulation considers an Eötvös number: $Eo = 288$, with density and viscosity ratios fixed at 10 and 1, respectively, and the Oh number set to 0.05. The numerical parameters are $Pe = 5$ and $Cn = 0.010$. As mentioned in [Section A.3.2](#), the reference velocity scale needed for the Péclet number can be chosen as $U_0 = \sqrt{g_y D}$ for gravity-driven flows. Also, dimensionless time can be defined by:

$$t^* = t \sqrt{\frac{g_y}{D}} \quad (23)$$

Our simulation results exhibit excellent agreement with the findings of Jalaal and Mehravaran (2012). As shown in [Figure 13](#), the comparison of the deformation of a liquid drop using both the Lattice Boltzmann Method (LBM) in 2D and the Volume of Fluid (VOF) method in 3D demonstrates that the evolution of the drop shapes over time is remarkably similar. For instance, at $t^* = 0.1647$, both methods capture the formation of a curved interface, and at $t^* = 0.3575$, the drop breakup into smaller droplets is observed in both approaches. This consistency across different numerical methods, with parameters set at $Eo = 288$, $Oh_h = Oh_l = 0.05$, and $\rho^* = 10$, validates the robustness and accuracy of our LBM simulations in replicating complex two-phase flow phenomena.

Overall, the dynamics of falling droplets involve complex interactions between buoyancy, inertia, and surface tension forces, leading to various deformation and breakup patterns, such as forming bags, ligaments, and secondary droplets. These phenomena are influenced significantly by the Eötvös number, with higher values leading to more pronounced deformations and faster breakup processes (Jalaal and Mehravaran, 2012).

A.3.4 RAYLEIGH-TAYLOR INSTABILITIES

The Rayleigh-Taylor instability (RTI) arises when a denser fluid is positioned above a less dense fluid in the presence of a gravitational field, causing the interface between the two fluids to become unstable. This phenomenon has been extensively studied due to its relevance in various natural and engineering contexts (Khanwale et al., 2023; Ren et al., 2016; Zu and He, 2013).

We consider a computational domain of size $[0, L_0] \times [0, 4L_0]$ with $L_0 = 256$ for our simulations. The initial interface is defined as $y_0(x) = 2L_0 + 0.1L_0 \cos(2\pi x/L_0)$. Periodic boundary conditions are applied on the left and right boundaries, while no-slip conditions are enforced at the top and bottom boundaries. The dimensionless numbers characterizing the RTI include the Atwood number, Reynolds number, Capillary number, and Peclet number:

$$\text{At} = \frac{\rho_H - \rho_L}{\rho_H + \rho_L}, \quad (24)$$

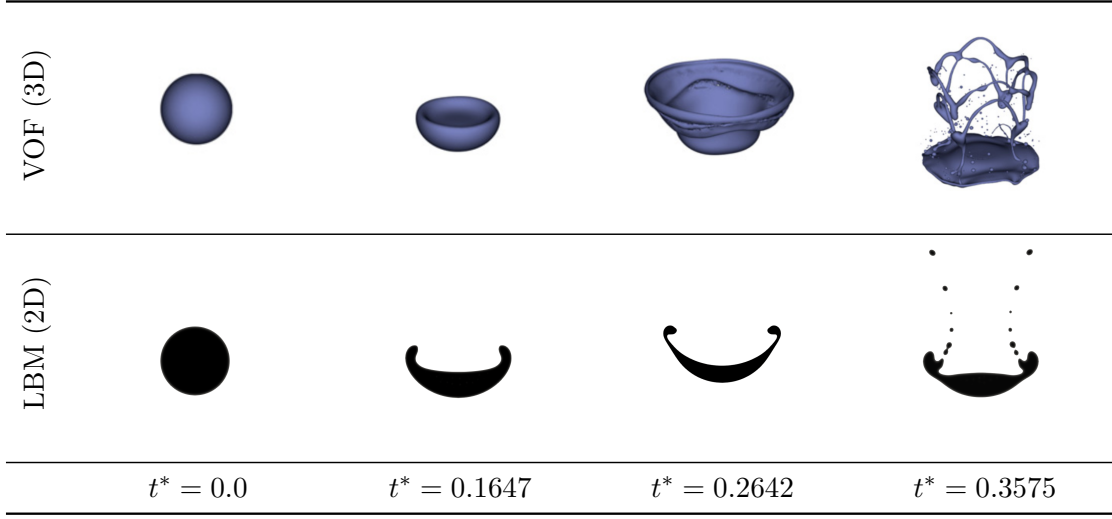


Figure 13: Comparison of the deformation of a liquid drop using the LBM and VOF methods: Current results and those of Jalaal et al. (2012) (Jalaal and Mehravaran, 2012) for $Eo = 288$, $Oh_h = Oh_l = 0.05$, and $\rho^* = 10$.

$$Re = \frac{\rho_H U_0 L_0}{\mu_H}, \quad (25)$$

where $U_0 = \sqrt{g_y L_0}$,

$$Ca = \frac{\mu_H U_0}{\sigma}, \quad (26)$$

$$Pe = \frac{U_0 L_0}{M}. \quad (27)$$

In our study, we used a density ratio $\rho^* = 3$, viscosity ratio $\mu^* = 1$, Reynolds number $Re = 128$, Atwood number $At = 0.5$, Peclet number $Pe = 744$, and interface width $\xi = 5$. The results are compared with the findings from Ren et al. (2016) and Zu and He (2013). The dimensionless time is defined as $t^* = t/t_0$, where $t_0 = \sqrt{L_0/(gAt)}$.

Snapshots of the interface evolution for the 2D Rayleigh-Taylor instability at different times are shown in Figure 14. Initially, the interface undergoes a symmetrical penetration of the heavier fluid into the lighter fluid, forming counter-rotating vortices. As time progresses, the heavier fluid rolls up into mushroom-like shapes, and secondary vortices form at the tails of the roll-ups. Our simulations' interface patterns and vortex structures are consistent with those reported in previous studies (Zu and He, 2013; Ren et al., 2016).

Appendix B. SciML Training

B.1 Model Hyperparameters

This section details the hyperparameters used for training the scientific machine learning (SciML) models. These parameters were carefully selected through extensive tuning to optimize model performance for the given datasets.

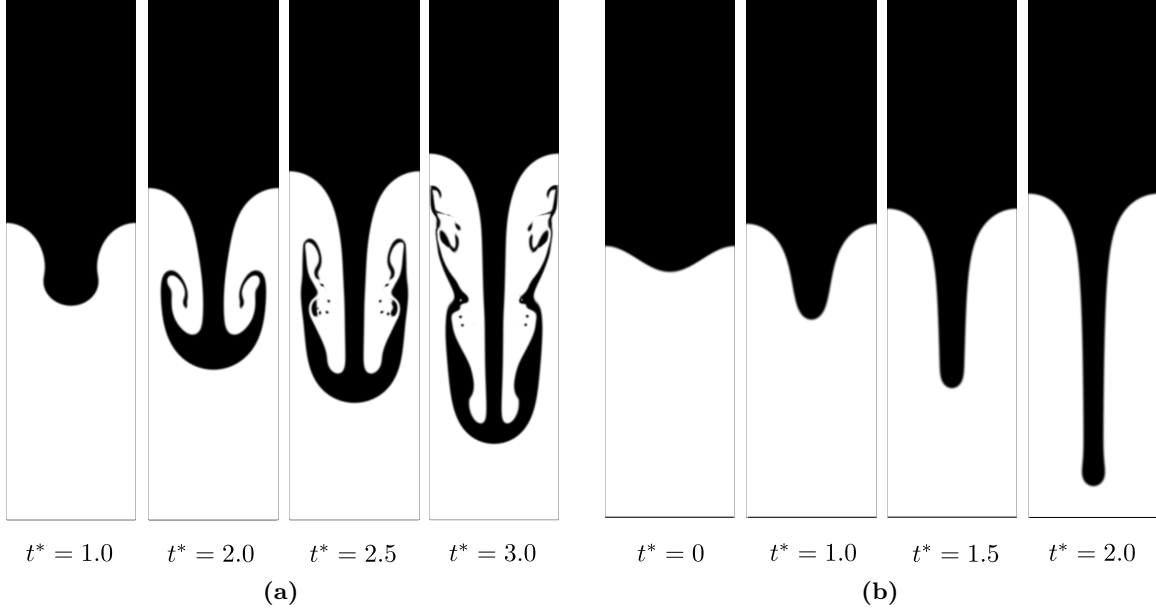


Figure 14: Evolution of the interface pattern of the 2D Rayleigh-Taylor instability for two scenarios: (a) $\rho^* = 3, \mu^* = 1, Re = 128, At = 0.500, Pe = 744, \xi = 5$; (b) $\rho^* = 1000, \mu^* = 100, Re = 3000, At = 0.998, Pe = 200, Ca = 8.7, \xi = 5$.

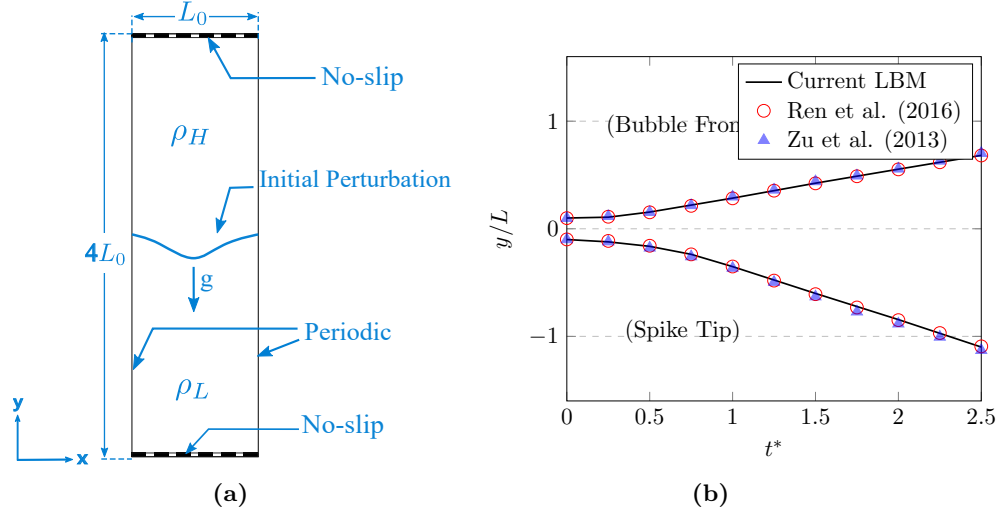


Figure 15: (a) Schematic of the initial setup for the Rayleigh-Taylor instability simulation, showing the boundary conditions and initial perturbation. (b) Comparison of the bubble front and spike tip positions over time for the Rayleigh-Taylor instability case with parameters $\rho^* = 3, \mu^* = 1, Re = 128, At = 0.500, Pe = 744$, and $\xi = 5$. The current LBM results (solid line) are compared with the results of Ren et al. (2016) (red circles) and Zu and He (2013) (blue triangles), showing excellent agreement in capturing the evolution of the instability.

• Fourier Neural Operator (FNO)

- Number of Fourier modes in both directions: 64

- Number of hidden channels: 32
- Projection channels: 32
- Number of layers: 10
- Learning rate: 0.0005
- **Convolutional Neural Operator (CNO)**
 - Number of layers: 4
 - Number of residual blocks (N_{res}): 6
 - Learning rate: 0.0005
- **DeepONet**
 - Branch network layers: [512, 512, 512]
 - Trunk network layers: [256, 256, 256]
 - Number of modes: 128
 - Learning rate: 0.0005
- **U-Net**
 - Encoder channels: [16, 32, 64, 128]
 - Decoder channels: [128, 64, 32, 16]
 - Learning rate: 0.0005
- **Poseidon**
 - Depths: [4, 4, 4, 4]
 - Embedding dimension: 48
 - Pretrained path: `camlab-ethz/Poseidon-T`
 - Learning rate: 0.0005
- **scOT**
 - Depths: [4, 4, 4, 4]
 - Embedding dimension: 48
 - Learning rate: 0.0005

B.2 Training and Validation Loss

To further analyze the training performance, the evolution of training and validation loss for four representative models (Poseidon-T and CNO) are shown in [Figure 16](#).

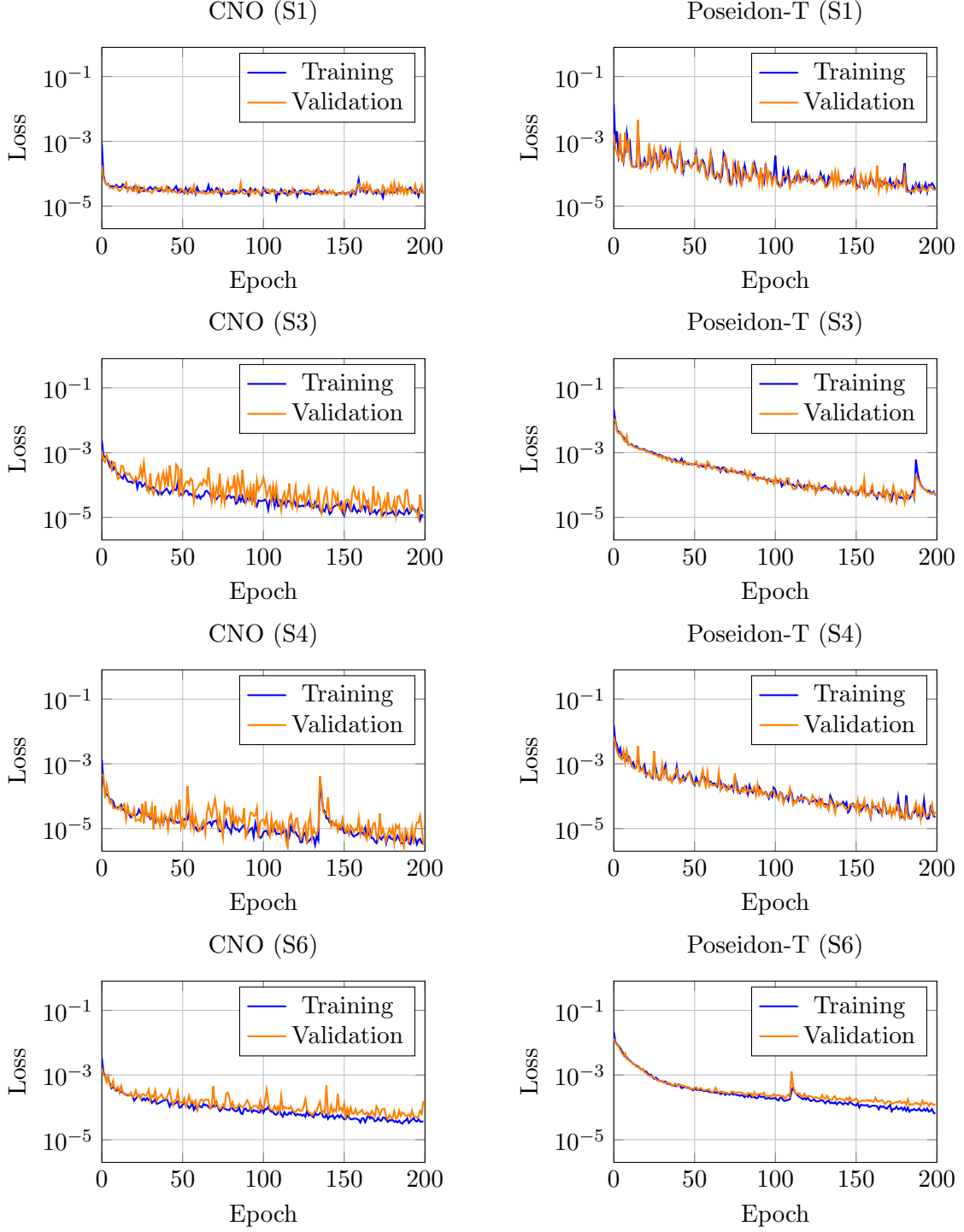


Figure 16: Training and validation loss (semi-log scale) for CNO (left) and Poseidon-T (right) across four different input-output mappings S1, S3, S4, and S6.